UNIVERSITY OF OKLAHOMA

GRADUATE COLLEGE

An Investigation and Solution to Spatial Interferers before RF Front End for Phased Arrays

A DISSERTATION

SUBMITTED TO THE GRADUATE FACULTY

in partial fulfillment of the requirements for the

Degree of

DOCTOR OF PHILOSOPHY

By

ROBIN IRAZOQUI
Norman, Oklahoma
2019

An Investigation and Solution to Spatial Interferers before RF Front End for Phased Arrays

A DISSERTATION APPROVED FOR THE
SCHOOL OF ELECTRICAL AND COMPUTER ENGINEERING

BY

Dr. Caleb Fulton, Chair

Dr. Nathan Goodman

Dr. Robert Palmer

Dr. Hjalti Sigmarsson

Dr. Christian Remling

This work is dedicated to my parents, Enrique Irazoqui and Ans Vloedgraven, who always believed in me, provided unconditional support, and pushed me to be my best.

Acknowledgements

This work would not have been possible without the contribution of others including Rodrigo Lebron, Jose Diaz, Javier Ortiz, Nick Peccarelli, and Dr. Saeedi who helped me accelerate the research process. I would like to thank Dr. Sigmarsson for his valuable advice throughout my PhD program. I am deeply grateful to Dr. Fulton, my advisor, for all the support he has given during the years we worked together. His mentorship was integral to helping me accomplish my goals. My brother, Pedro Irazoqui, helped me expand my horizons by inviting me to the USA to do my first internship which led to my ending up at the University of Oklahoma. Finally, Jaclyn Talarico, my girlfriend, provided love and patience, and graciously gave of her time to read, edit, and help improve this work.

Table of Contents

List of Figures

Abstract

Fully digital arrays offer significant advantages in terms of flexibility and performance, however they suffer from dynamic range issues when used in the presence of in-band interferers. Higher dynamic range components may be used, but are more costly and power-hungry, making the implementation of such technology impractical for large arrays. This paper presents a way to mitigate those interferers by creating a spatial notch at the RF front-end with an antenna agnostic circuit placed at the feeding network of the antenna. This circuit creates a steerable null in the embedded element pattern that mitigates interferers at a specified incoming angle. A full mathematical model and closed-form expressions of the behavior of the circuit are obtained and compared to simulated and measured results. Up to 20 dB null in the embedded element pattern of a 1x8 array is achieved with less than 1.5 dB of insertion loss. A steerable null using phase shifters is shown to prove real-time changes in the null placement. Phase shifters are substituted by tunable filters and enable a significant boost in the overall performance. To further validate the concept, a real case scenario is set up with a desired signal and an interferer that is initially saturating the receiver. The receiver successfully demodulates the signal after the null is placed in the direction of the interferer. The circuitry is then expanded to a planar array to fully optimize the interferer-free scanning volume.

1 Introduction

Phased arrays were first investigated in 1950 and through continuous improvement have come to serve in areas such as electronic warfare and wireless communications [1],[2]. In recent years, there has been an increased interest in fully digital arrays that are low-cost, reconfigurable and allow multifunction capabilities. This type of array has been explored for decades and has been advanced by improvements in silicon-based technology [3]. In phased arrays each element radiates a wide-beam of electromagnetic waves that has a phase distinct from its neighboring elements (progressive phase shift). For a sufficient electric distance (far field), the electromagnetic waves add up constructively in a certain direction, called the main beam. Simultaneously, the electromagnetic waves combine destructively in a different direction, resulting in sidelobes and nulls. When the progressive phase shift changes, the electromagnetic waves will then add up constructively in a different direction, effectively changing the angle of the main beam. The action of changing the direction of the main beam is known as beamsteering. Traditional analog phased arrays perform beamforming at the RF front-end and usually use a component called a phase shifter. The purpose of the phase shifter is to add a group delay to the signal at the RF stage and change the phase of the RF signal. Next generation arrays will be fully digital, meaning each element is digitized, and the array will thus be capable of digital beamforming (DBF) [4]. Digital beamforming opens the door for a new level of precision, reconfigurability, and expanded functionality that cannot be achieved with analog beamforming. These advantages permit levels of flexibility in radar such as adaptive digital beamforming for jammer suppression and space-time adaptive processing (STAP) for ground moving target indicating radar [1]. These advantages also apply to the wireless communication industry in which spatial multiplexing allows for more efficient spectral/spatial management and results in higher

data-rate.

In addition to precise beamforming, digital arrays offer other advantages, such as "in-situ" calibration, higher dynamic range, and an improvement of phase noise [4], [5]. Experimental setups of digital arrays were first investigated in [6] when digital beamforming was done for a linear array. Authors in [7] explored using a 2x4 array built with commercial off-the-shelf (COTS) components. Two dimensional beamforming was demonstrated in an experimental 8x8 setup in [8]. Fully digital arrays have been developed in recent years with the purpose of further exploring their advantages. A CEAFAR S-band radar in Australia [9] is claimed to have extremely low weight and low cooling power and an EL/M-2248 MF-STAR in Israel [10] is used for multiple target detection and radar missile guidance. Both the Australian and Israeli radars were developed for their naval forces. Currently the U.S. Office of Naval Research (ONR) is also developing a fully digital array, the FlexDar testbed.

More recently, the FAA and NOAA developed a multifunction phased array radar (MPAR) program that combines weather surveillance and air traffic control, as well as other missions [11]. Another recent project has been developed by DARPA Arrays at Commercial Timescales (ACT) where they are working on scalability and cost reduction of digital arrays by using modular common tiles [12]. The academic world has made progress with digital arrays. For example, two achievements accomplished at Purdue University, the developer of the Army Digital Array Radar (DAR), a 16 element S-Band radar made with COTS components, were cost reduction and self-calibration [1]. The University of Oklahoma is working on Horus, which is an 8x8 fully digital dual polarized array using COTS transceiver AD9731 chip [13]. Dual-polarization improves measurements and weather characterization but high isolation is required between polarizations [14], [15].

Some serious challenges to successful implementation of digital arrays will be achieving low energy consumption and low-cost per antenna element [16], [17]. Independently controlling and digitizing each individual antenna element allows maximum flexibility, but it is achieved at the cost of an increased need for digital processing power and therefore, electric power consumption. Compared to analog arrays that have only one transceiver, and thus one data stream, digital arrays need larger processing power because of the increase in the number of transceivers and the necessity of handling the high data rates produced [3]. Traditional analog phased arrays beamform N antenna elements in the analog domain, and the result of the "summed" signal is then digitized in one single receiver. A fully digital array has one transceiver per antenna element, therefore it requires the same amount of receivers as the number of array elements, which increases its cost and energy consumption by a factor of N compared to the analog phased array. Recent developments in silicon-based integrated circuits have allowed for great technical improvements that lower power requirements and the price of components, thus reducing the overall costs of digital arrays [17],[18]. Despite these improvements, the power requirements and costs of fully digital arrays are still a limitation for general implementation, especially when compared to traditional phased arrays. These limitations are present despite the fact that digital arrays do not need phase shifters, an expensive component of traditional phased arrays.

In addition to DBF and "in-situ" calibration, an improvement of up to $10log(N)$ dB in the phase noise and dynamic range is expected when combining N receivers [5]. Combining receivers relaxes the dynamic range requirements for the analog-to-digital converter (ADC). Relaxing the dynamic range translates into a reduction of bits needed, and therefore reduces the cost and power consumption [6],[19]. Problems, in terms of dynamic range, arise for fully digital array receivers when

strong interferers are present in the environment, whereas traditional phased arrays do not have this limitation, as shown in Figure 1.1. The reason such problems do not arise in traditional phased arrays is because they beamform in the analog domain where out-of-beam interferers are mitigated through destructive interference before digitization. In digital arrays, beamforming is done in the digital domain, thus, the receiver array will not benefit from the array factor in the analog domain in the way that traditional analog phased arrays do. As a result of this, higher dynamic range ADCs are needed to resolve a weak signal in presence of a strong interferer [20]. Strong interferers can drive the active components into the non-linear region of operation, or even saturation, consequently significantly degrading the quality of the desired signal.

When the strength of the signal drives the active devices into compression, the main signal and its spurious products also get digitzed. The compressed signal and the resulting spurious products are beamformed in the digital domain as illustrated in Figure 1.2. Spurious products can add up coherently within a certain scan angle and create a false positive target during digital beamforming [18],[21].

Since dynamic range and non-linearities are the main limitations in the implementation of large fully digital arrays, the author would like to emphasize the previously discussed importance of dynamic range and summarize it. The lack of spatial filtering allows for interferers to enter unmitigated into the receiver, necessitating more linear components in the receiver chain, which are more expensive. Most importantly, transceivers need a higher dynamic range ADC per channel, which translates into a drastic increase in price and power consumption.

A recent survey of spatio-spectral interferers and non-linearities focused on 5G MIMO wireless systems was done tangentially to the work presented here [21]. The survey provides an in-depth examination of modelling and correction of non-

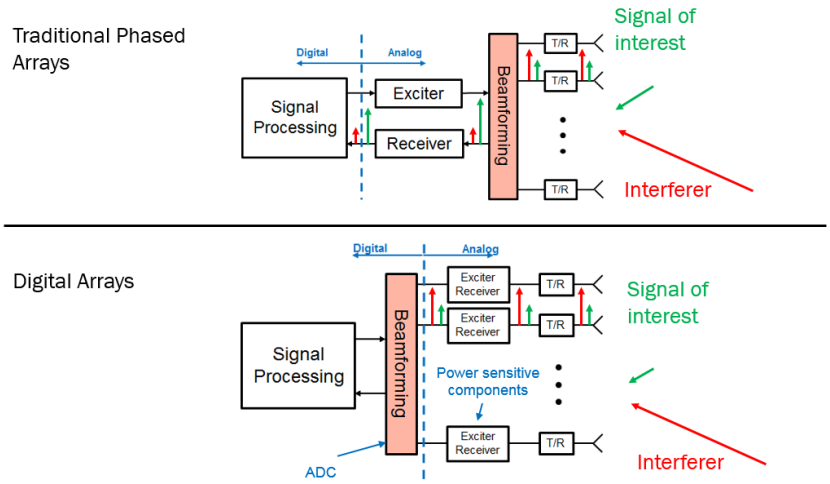

Figure 1.1: An illustration of how a signal goes through the receiver chain for a traditional phased array and fully digital arrays. The goal is to show how the interferer goes unmitigated into the digitization block.

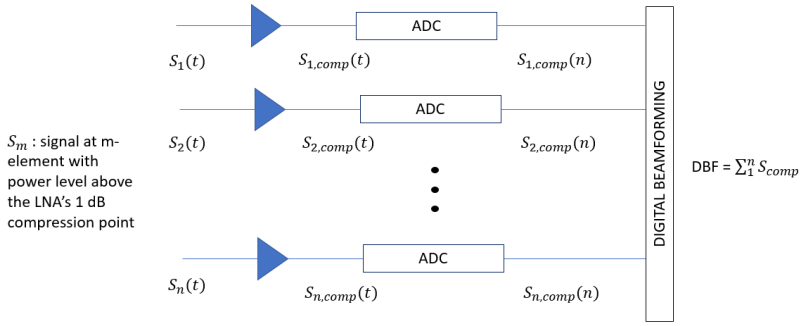

Figure 1.2: A block diagram illustrating a strong signal that compresses the LNA and gets digitized and beamformed.

linearities for an improved dynamic range. For example, research in digital post distortion has been done to improve the dynamic range of a receiver in the presence of RF interferers that produce higher order intermodulation products in the receiver chain that corrupt the desired signal [22]. This technique linearizes the signal and conditions it for further processing. Usually non-linear equalization (NLEQ) techniques are applied to the first and most critical component of the receiver chain to mitigate its distortion. Usually that critical component is a low-noise amplifier

(LNA), although recently, correction has also been expanded to other non-linear components, such as a tunable filter [23]. NLEQ techniques have been proven to be effective only under weak non-linearities, but better solutions are needed to solve this issue for strong interferers.

There is a clear need to provide robust interference mitigation when considering the requirements of fully digital arrays which, over time, are subject to an increase of interference due to spectrum cluttering and the need for optimized spatial-spectral efficiency. Since the advantage of digital arrays is to be able to capture the whole scanning volume at once, it would be ideal to be able to remove the interferer while preserving as much of the whole scan volume as possible (interferer-free scanning volume). Figure. 1.3 is an illustration of the spatial response to an interference, where the direction of the interferer is mitigated (and can possibly be characterized) and all other angles remain unmitigated, allowing for the desired signal to enter into the receiver unmodified. An intuitive way to solve the problem of interference is to place a narrow null in the spatial response. Ideally, this spatial and spectral interference mitigation would occur at the antenna element itself, before any active electronics are involved. Mitigation at the antenna level would relax the dynamic range requirement for ADCs and allow the use of devices with a lower P1dB compression point that are usually more cost effective. Reducing the cost of active components would not only benefit fully digital arrays, but also the components that are located between the antenna and the beamformer in traditional phased arrays,

This work introduces a novel antenna agnostic circuitry that provides spatial interference mitigation before the RF front-end by placing a steerable null in the embedded element pattern. Despite the impact that spatial interferers have on digital arrays, there has yet to be a solution that provides spatial interference mitigation

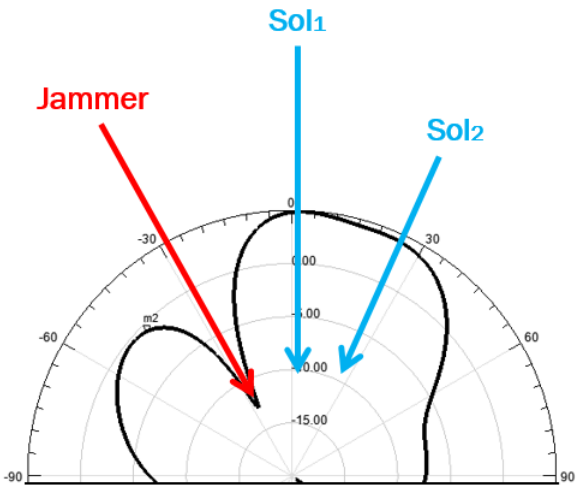

Figure 1.3: An illustration of an embedded element pattern where there is a null placed at the incoming angle of the jammer while letting through the signal of interest from the other angles.

at RF while simultaneously being antenna/receiver agnostic. The current work proposes a circuit designed to solve interference problems. This circuit is composed of well-known, simple RF components in a design that is easy to implement. As shown in the next section, there have been many attempts to mitigate spatial interferers in various ways, but none of them provided a solid, general solution applicable to any array architecture.

1.1 Antenna Patterns and Beamforming

Previous sections explain the importance of being able to reduce interference before it reaches the receiver front end, necessitating mitigation at the radiating layer itself or within the feeding network, both of which can have an impact on the antenna pattern. Knowledge of the basic concepts of beamforming is needed to further understand the advantages of nulling in the antenna pattern. To increase the radiation of an antenna in a certain direction (gain), the dimensions of the antenna itself need to expand, thereby increasing its equivalent electrical length. A simple way to in-

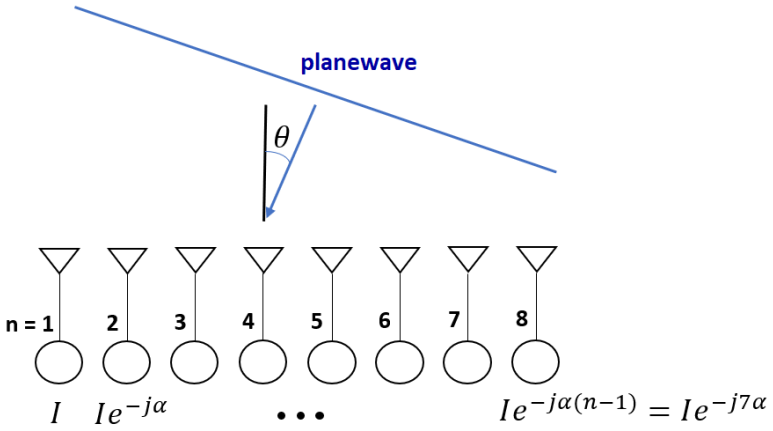

Figure 1.4: Illustration of a planewave illuminating an 8 element linear array and inducing currents that have an equivalent magnitude of I, but due to the incoming angle θ have a different phase defined by the progressive phase shift.

crease the electrical dimensions of an antenna is by distributing smaller antennas over a surface, creating an array. When the antenna array receives a planar electromagnetic wave, it creates excitations for each radiating element. Those electrical excitations are added together, emulating an electrically large antenna. When a planewave comes in off-broadside excited antenna elements will each have a different phase. In Figure. 1.4, a 8 element linear array is shown with a planewave illuminating the array at an angle θ away from broadside. In that same figure, element 8 receives the signal first and has a different phase with respect to the other elements. These signals need to be corrected in phase in order to be able to add them coherently. This phase correction is what is known as applying a progressive phase shift $\alpha(n-1)$.

One easy way to understand how antenna arrays work is to visualize the array operating in transmit mode, because antennas are passive and reciprocal. When all elements are excited, the antenna pattern is the result of the contribution of the electrical field of each individual element.

$$\vec{E}(r,\theta,\phi) = \sum_{n=1}^{N} \vec{E_n}(r,\theta,\phi) \tag{1}$$

where each $\vec{E_n}(r,\theta,\phi)$ is the electric field of each antenna element and can be expressed as

$$\vec{E_n}(r,\theta,\phi) = |I_n|e^{-j\alpha(n-1)}\vec{e_n}(r,\theta,\phi)e^{jk(n-1)dcos(\theta)} \tag{2}$$

The first term, $|I_n|e^{-j\alpha(n-1)}$ in (2), represents the excitation of each element and its progressive phase shift, as defined by $\alpha(n-1)$. The term $e^{jk(n-1)dcos(\theta)}$ in (2) represents a contribution to the delay in phase due to its position in the array. The term $\vec{e_n}(r,\theta,\phi)$ in (2) represents the embedded element pattern of the array and contributes to defining the magnitude of the signal as a function of the incident angle (θ,ϕ). In this case, mutual coupling and edge effects are all embedded in this term. The goal is to manipulate $\vec{e_n}$ in such way that its magnitude is very small for a certain $(\theta_{null},\phi_{null})$, resulting in a total electric field that tends to 0 V when beamforming in that direction using (1). Beamforming for different angles when there is a null in the embedded pattern is illustrated in Figure. 1.5, where an 8 dB null was created in the embedded element pattern for $\theta = 0$ (stop-angle). When beamforming at broadside, there is more than 8 dB of gain difference between the array that has no null (solid lines) versus the array that has the null in the embedded element pattern placed at broadside (dashed lines). When beamforming away from broadside, the solid lines and dashed lines closely match, implying that there is no mitigation for those angles (pass-angles).

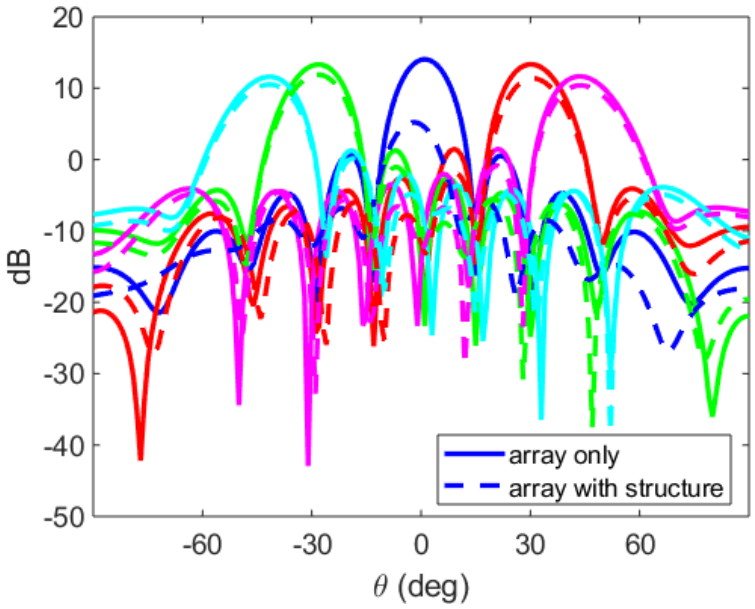

Figure 1.5: Illustration of beamforming for a regular "naked" 8 element linear array (solid line) and beamforming when there is a 8 dB null in the embedded pattern at broadside (dashed line).

1.2 Noise Figure, Dynamic Range and Spurious Free Dynamic Range

Noise figure is critical to the performance of any RF system. It determines the minimum amount of power an incoming signal needs to have in order to be detected by the receiver. Noise can be either captured by the environment or it can be internally generated by the RF components in the receiver chain. Noise power is produced by random thermal vibrations generated in any component operating at a temperature above absolute zero [24]. These random processes significantly contaminate the signal if the signal strength is low enough. The point of contamination is determined by the noise floor of the RF system. It is highly desirable to reduce the noise floor as much as possible to maximize the receiver sensitivity. The noise induced by components is commonly represented as

$$N_0 = T_e G k B \tag{3}$$

where T_e is the equivalent noise temperature of a component. A higher temperature creates the conditions for more powerful random processes resulting in a higher noise floor. $k = 1.38 \times 10^{-23}$ is the Boltzmann's constant in (J/∘K). G is the gain of the component and B is the bandwidth. The noise figure is a relative measurement of the signal-to-noise ratio (SNR) increase when the signal passes through a component that has a certain noise temperature

$$F = \frac{S_i/N_i}{S_0/N_0} \tag{4}$$

When a signal goes through a cascade of components, the total noise figure is expressed as

$$F = F_1 + \frac{F_2 - 1}{G_1} + \frac{F_3 - 1}{G_1 G_2} + ... \tag{5}$$

Therefore, the dynamic range can be expressed as the ratio of the maximum power that the receiver can handle and the noise floor. The maximum allowed power of an incoming signal is determined by the gain compression of the most sensitive component. Gain compression is caused when the device enters the non-linear zone due to a high input signal. Harmonics called intermodulation products start to appear when driving active devices into the non-linear zone. When the signal has a certain bandwidth, or is composed of multiple tones, the intermodulation products can fall within the bandwidth of the system. The harmonics grow more rapidly in power than the linear tone. The higher the order of the intermodulation products, the quicker they grow. If the signal drives the component into compression, intermodulation products can appear above the noise floor. This can contaminate the

signal of interest and can create false targets during digital beamforming [23]. The spurious-free dynamic range is the ratio of maximum power that the system can handle before spurious products appear above the noise floor, and the noise floor itself. Usually signals of interest do not cause the system to go into compression, but strong interferers can. This is one of the reasons that being able to prevent the interferer from entering the receiver chain is so important.

1.3 Current Technology and Research

As previously mentioned, it is most desirable to have spatial interference mitigation at the antenna elements themselves. In recent years, many advances have been made at the element and array levels in the field of pattern reconfigurable antennas (PRAs), but all research has been focused on trying to create a way to steer a beam at element level [25]-[28]. Investigation of PRAs at the array level has been done in [29]. A non-planar structure that is able to scan more than 180° was described in [30]. A full cylindrical array providing the ability to scan a complete 360° has been proposed in [31]. PRA research has been more focused on beamsteering rather than trying to null specific angles where signal interferers are located. One drawback of PRAs is that their electrical size is larger than half-wave length ($\lambda/2$). This means that unwanted grating lobes occur in the visible region. An interesting focus for future research might be investigating types of PRA structures that allow nulling while maintaining a traditional $\lambda/2$ element size in order to avoid the difficulties that would arise at the array level.

Another way to handle spatial interference is by using the Butler matrix. It was first introduced in 1961 [32], but has recently awakened interest in the MIMO community because it has the ability to simultaneously generate fixed beams in different directions to cover the whole scanning range. The architecture combines lossless

passive devices, mostly quadrature hybrids and fixed phase shifts. The Butler matrix provides a cost-effective solution to beamforming, but the main tradeoff is its lack off flexibility when beamforming. Side lobe level suppression is compromised because there is equal power for each element and no tapering can be done effectively. Research mitigating sidelobe levels has been investigated in [33] but the results obtained are orders of magnitude worse than digital tapering, and the solutions proposed add extra complexity to the system. Despite the lack of flexibility and high sidelobe levels, the main concern of the Butler matrix technology is its scalability since all components are interconnected at some point throughout different stages. The lack of scalability makes the complexity increase exponentially for large arrays. Efforts in reducing the complexity have been tackled by miniaturizing the Butler matrix with complex 3D waveguides [34], lumped components [35] or an RFIC for an 8x8 array [34].

Research in the integrated circuits (IC) domain has investigated using active electronics in the RF front-end and baseband sections. For example, a full four-element integrated MIMO receiver array with 8 dB spatial interference mitigation at the RF front-end, and another 24 dB of cancellation at baseband before digitization was developed in [17]. A total of 51 dB mitigation with moderate impact in the noise figure of $3.4-5.8$ dB and the ability to create multiple notches is demonstrated in [36]. This approach implies designing a fully integrated receiver resulting in lack of flexibility because the RF system must use only that specific receiver architecture in order to have a front-end spatial filter. Other approaches, such as having a beamformer integrated in the LNA were presented in [37]. The beamformer selects the interferer and feeds it deconstructively into the amplifying stage of the LNA to cancel out the interfering signal. Mitigation of up to 20 dB of attenuation was achieved with a noise figure of 12 dB, thereby impacting the sensitivity of the re-

ceiver. Both approaches use complementary metal-oxide-semiconductor (CMOS) technology that compromises the power handling limitation when strong interferers are present. These CMOS RF front-end architectures suffer from a trade-off between noise figure and power handling. This trade-off is caused because high gain is needed at the RF front-end to reduce the noise figure, but due to low supply voltages used in current CMOS processes, even a 0 dBm interferer will can cause the amplification stage to clip and will result in a dynamic range limitation [38]. Adaptive digital beamforming (ADBF) digitally cancels the interferers that are present in the signal, but under the assumption that the individual receivers have not been compressed; otherwise, spatial correlation can create distortion products that are in the direction of the signal of interest, even if the interference sources are far away [5]. ADBF needs extra processing, and it can be slow to adapt to changes, making it less effective for dynamic clutter or interference. It is especially computationally intensive when performed at the element level [18].

Destructive interference was used to cancel out mutual coupling effects for simultaneous transmit and receive applications in [39]. Interconnected transmit and receive antennas with directional couplers achieved an isolation of almost 10 dB. Interconnecting antenna elements to improve scanning range in arrays was accomplished using direct connections [40], and directional couplers [41] in which the active impedance matching versus scan angle is improved by cancelling the mutual coupling effects of their adjacent elements. Destructive interference at the radiating layer using mutual coupling mechanisms has not yet been used to mitigate spatial interferers. These concepts are relevant because the circuitry presented in this work is based upon interconnecting adjacent elements.

1.4 The Spatial Interference Mitigation Circuitry (SIMC)

This work introduces an RF circuit that is able to mitigate interferers at the RF front-end before they enter the receiver by creating a steerable null in the antenna's embedded element pattern. This circuitry is made out of well-defined and non-complex components including a quadrature hybrid and transmission lines. Tunable circuitry is needed to steer the null in different directions. The most common placement of the proposed circuitry is to locate it at the antenna feeding network. This is highly convenient because it means that the spatial interference mitigation circuitry (SIMC) is able to place the null before the interferer enters the receiver chain. Another benefit is that it does not affect the design of the antenna array or any of the receiver's hardware. This circuitry directly impacts the dynamic range proportional to the depth of the null, allowing the use of ADCs and other components that have a lower dynamic range, thus reducing costs and power consumption.

This work mathematically proves that this technique is antenna agnostic for large arrays and can be implemented with practically any array. It also means that it can be placed at any stage of the RF layer. This flexibility would be useful, for example, in cases where high sensitivity is needed and an LNA could be placed before the circuitry, reducing the system's noise floor. Since the theoretical circuitry is made of passive components (it needs active components for a steerable null) it implies that the circuit is reciprocal and therefore it can work on either transmit or receive. The theoretical analysis is discussed in chapter 1, where the SIMC is explained and applied to a linear array and the mathematical model for an infinite array is derived. The mathematical results will allow defining the parameters for the SIMC such that it places the null at the desired scan angle. Simulation results using a full-wave finite-element method simulator, provided by ANSYS HFSS, are then used to verify the validity of the mathematical model for the unit cell conditions.

Chapter 2 introduces the fundamental theory of the SIMC and derives a closed-form expression that accurately predicts the null placement and the physical properties needed to achieve that placement. The need for linearity and dynamic range improvement in digital arrays is especially present in large arrays because of the scaling of costs. As the circuitry is intended for large arrays, the infinite array approach is used to describe the system because it has the advantage of simplifying the mathematical modelling while simultaneously maintaining accurate results. The resulting closed-form expression is then further analyzed with the goal of improving system level performance.

A finite array is needed in order to fabricate and obtain measured results. Chapter 3 covers the design, prototyping, and measurements of the SIMC when applied to a 1x8 array. As mentioned previously, an active component is needed for the null to be steerable. Initially, a phase shifter was used to steer the null. Embedded element patterns were extracted, and nulls of more than 20 dB were achieved. After measuring successful nulls, the whole array was tested in a controlled real case scenario composed of a strong interferer and a signal of interest (SoI). The strong interferer prevented the receiver from correctly demodulating the QPSK format of the SoI. When the null was placed in the direction of the interferer, the receiver could then successfully demodulate the signal. The phase shifters used had more than 7 dB of insertion loss (IL) degrading the noise-figure significantly from less than 1 dB (ideal case) to more than 5 dB for the phase shifter case. Because the SIMC was designed and tested for a linear array, the null is one dimensional and cuts a whole angular plane. For example, if the null was set for 20°, it would mitigate the whole plane regardless of the elevation angle, resulting in an important information loss.

A null that cuts a whole plane is far from ideal. Chapter 4 aims to fix this

problem by redesigning the circuitry that enables the placement of a "pinpoint" null. This new circuitry is an evolution of the one proposed in chapter 2 and is able to generate a null at any specified (ϕ, θ). This nulling improvement is an important advancement because it maximizes the interferer-free scanning volume. A 2D array needs to be designed in order to achieve both of these improvements. Therefore, a 7x7 array is designed and prototyped, and pinpoint nulls of more than 20 dB rejection at the stop-angle are measured. Despite using infinite array analysis, the mathematical model that is derived is far more complex than the model derived for a linear array. The expression accurately predicts the null placement when the physical properties are set. An iterative method is needed for a reversed scenario in which the user defines the null placement and the derived formula transforms it into physical properties of the planar SIMC (2DSIMC).

Chapter 5 focuses on the tremendous advantages to the SIMC when the 'tunable component' has a reduced IL. As seen in chapter 2, a reduced IL improves the overall IL of the system and provides a more selective null. The tunable component developed in chapter 5 is a second order tunable filter. Filters are usually measured by IL, out-of-band slope, and rejection, but rarely for the phase response. This work presents a SIMC with a tunable pass-band filter. The phase of the filter at the operating frequency of the system will vary when changing the center frequency of the tunable filter. The filter acts as a low-loss phase shifter. It was mathematically proven and later confirmed with simulations that a low-loss filter decreases the noise figure to less than 0.4 dB.

2 Spatial Interference Nulling Technique

The final goal of this research is to apply spatial interference mitigation to large arrays. Therefore, an infinite array approach was chosen to derive the mathematical model to describe a front-end spatial interference mitigation circuit (SIMC) and predict where the nulls are placed in the spatial domain. The performance of a large finite array can be precisely modeled using infinite array theory because it assumes that all antennas have equal embedded element patterns, the edge effects are negligible, and mutual coupling is embedded in one variable called the active reflection coefficient. The mutual coupling is treated through the use of floquet ports and master/slave boundary conditions [42]. The traditional way to describe an infinite array environment is by using the definition of a unit cell [42]. A unit cell defines the electromagnetic properties of a single radiating element when it is placed equidistant from copies of itself that form an infinite array. The unit cell equivalent schematic is shown in Figure 2.1a, in which the only difference between adjacent unit cells is the progressive phase shift ϕ. The antenna feeds the received signal directly into the mitigation circuit. This circuit is composed of an undefined two-port network for which properties need to be designed in order to generate a null for a certain angle of incidence connected with a quadrature hybrid. This SIMC is placed in a layer that goes between the radiating element and the transceiver's front-end. In Figure 2.1a the quadrature hybrid interconnects the antenna's port (Port 2) with the transceiver's front-end (Port 1). Since one of the properties of the quadrature hybrid is to split its power, the resulting wave at Port 3 is used to feed the cancelling signal into its adjacent element through the two-port network. This two-port network modifies the cancelling wave in gain and phase in such a way that it adds destructively into its adjacent element through Port 4 in order to achieve a null for a desired scan angle. The SoI coming from different angles will go into

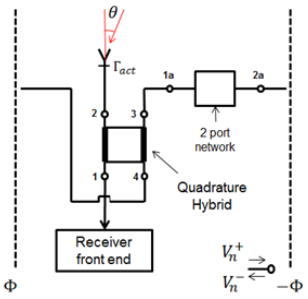

(a) Equivalent Schematic

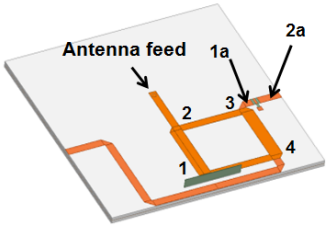

(b) Top View

(c) Bottom View

Figure 2.1: An illustration showing (a) unit cell schematic, (b) equivalent 3D model for top layer, (c) 3D model for bottom layer.

the adjacent element through the two-port network and will feed constructively. Its equivalent physical structure is shown in Figure 2.1b where it is connected directly to the via-fed patch antenna shown in Figure 2.1c. The two layers are separated by a ground plane.

2.1 SIMC Mathematical Modelling for a Unit Cell

Scattering Matrix analysis is used to describe the mathematical model, where a quadrature hybrid S-parameter matrix is nominally given as

$$\left|S_{quadrature\ hybrid}\right| = \frac{1}{\sqrt{2}} \begin{vmatrix} 0 & -j & -1 & 0 \\ -j & 0 & 0 & -1 \\ -1 & 0 & 0 & -j \\ 0 & -1 & -j & 0 \end{vmatrix} \tag{6}$$

The two-port network from the right side of Figure 2.1a in its general form can be defined as

$$\left|S_a\right| = \begin{vmatrix} S_{11a} & S_{12a} \\ S_{21a} & S_{22a} \end{vmatrix} \tag{7}$$

where $S_{11a} = S_{22a} = 0$ because perfect matching is assumed. For simplicity, the initial assumption is that the two-port network is symmetric, therefore $S_{12a} = S_{21a} = G \cdot e^{-j\theta_2}$. The gain and phase of this two-port network is what needs to be designed in order to produce a null for a certain scan angle. Under these assumptions, and denoting the incident and reflected voltages with + and - subscripts, respectively, expressions like the following can be obtained for when operating in receive mode

$$V_1^- = V_2^+ S_{12} + V_3^+ S_{13} \tag{8}$$

$$V_3^+ = V_{1a}^- \tag{9}$$

$$V_4^- = V_2^+ S_{42} + V_3^+ S_{43} \tag{10}$$

$$V_{1a}^- = S_{11a} V1a^+ + S_{12a} V_{2a}^+ \tag{11}$$

$$V_{2a}^+ = V_4^- e^{-j\phi} \tag{12}$$

ϕ is the progressive phase shift produced at each antenna element for an incoming wave at an angle θ away from broadside. The relationship between these two values for a linear array can be expressed as

$$\phi = kd\sin(\theta) \tag{13}$$

Where k is the wave number and d is the distance between elements. Since this SIMC is antenna agnostic, the performance of this circuitry can be better extracted when the antenna and its mutual coupling effects are not taken into consideration,

therefore $V_2^+ = 1$ V. Note that the same equations can be used for transmit with the assumption that

$$V_1^+ = 1V \tag{14}$$

V_1^- is the voltage going into the transceiver, as shown in Figure 2.1a, and a closed-form expression for V_1^- can be calculated for an incoming wave, resulting in

$$V_1^- = \left[S_{12} + S_{13} \frac{S_{12a} S_{42} e^{-j\phi}}{1 - S_{12a} S_{43} e^{-j\phi}} \right] \tag{15}$$

From the above expression it is clear that the voltage going into the receiver is dependent on the properties of the quadrature hybrid, the S-parameters of the two-port network, and the progressive phase shift ϕ through out the array due to a plane-wave arriving at an incoming angle. The goal is for that voltage to be zero for a certain scan angle and S_{12a} can be extracted by solving $V_1^- = 0$ in (15). A closed-form expression is obtained for S_{12a}

$$S_{12a} = \frac{S_{12}}{S_{12} S_{43} - S_{13} S_{42}} e^{-j\phi} \tag{16}$$

In order to create the null for a certain scan angle θ, ϕ needs to be set using (13) and the gain and phase can be obtained from (16). The magnitude of S_{12a} will remain constant for different null placements along θ and it is only dependent on the S-parameters of the quadrature hybrid. The gain will be $|S_{12a}| = 1/\sqrt{2}$ (or a 3 dB attenuator) for an ideal equal split quadrature hybrid.

Once the S_{12a} is calculated from (16), the response of the signal going into the receiver versus the incident angle can be calculated by using the expression derived in (15). The response of the SIMC for three different nulling angles ($-43°$,

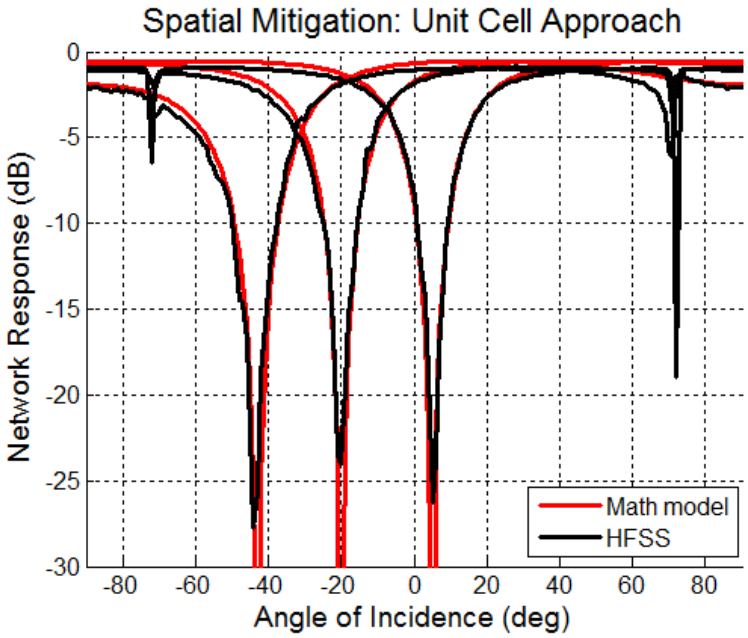

Figure 2.2: Comparison between the mathematical model (red) and HFSS simulations (black) of the signal going into the receiver versus scan angle.

$-20°$ and $5°$) is shown in Figure 2.2 where the red traces are the predicted spatial responses produced when plotting (15) for $-90° < \theta < 90°$. At the stop-angle, the signal gets successfully deconstructed for the incident angle where the null is needed. At the pass-angle, the signal from its adjacent element adds constructively with the signal produced by the excitation decreasing the IL to 0.5 dB.

2.2 Performance Optimization and System Level Analysis

The mathematical model proves that it is theoretically possible to place a null in the spatial domain and mitigate the interferer before it reaches the RF front-end. It would be highly beneficial if the SIMC could provide a higher level of flexibility, such as being able to change the null width and manipulate the overall IL. In the previous section, a regular equal power split quadrature hybrid was assumed. This quadrature hybrid equally divides the power passing through port 1 between ports

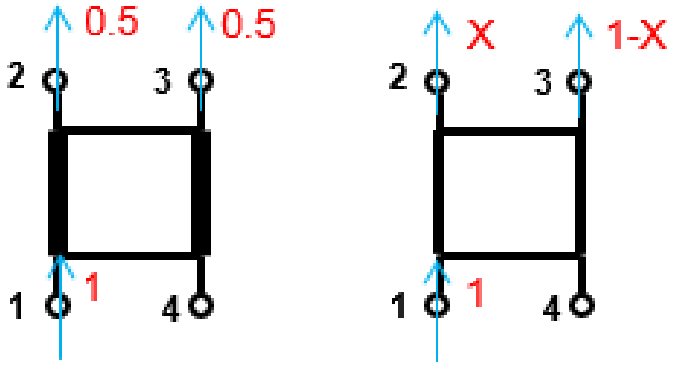

(a) Equal Split (b) Unequal split

Figure 2.3: Illustration of a schematic of (a) an equal split quadrature hybrid and (b) an unequal split quadrature hybrid.

2 and 3. The response from (15) is a function of the S-parameters of the quadrature hybrid, and V_1^- can be modified when using unequal split quadrature hybrids.

It is necessary to verify that unequal power splitting is theoretically possible by satisfying the conditions defined by the unitary matrix. The reason for this is that quadrature hybrids are reciprocal (symmetric) and lossless. In terms of S-parameters, in order for a component to be unitary, it needs to follow that

$$\sum_{k=1}^{N} S_{ki} S_{ki}^{*} = 1 \tag{17}$$

$$\sum_{k=1}^{N} S_{ki} * S_{kj}^{*} = 0 \tag{18}$$

for $i \neq j$. The quadrature hybrid can be expressed in its general form as

$$\left| S_{quadrature\ hybrid} \right| = \frac{1}{\sqrt{2}} \begin{vmatrix} 0 & S_{12} & S_{13} & 0 \\ S_{21} & 0 & 0 & S_{24} \\ S_{31} & 0 & 0 & S_{34} \\ 0 & S_{42} & S_{43} & 0 \end{vmatrix} \tag{19}$$

Knowing that a quadrature hybrid is a symmetrical passive device, the S-parameter matrix can be rewritten as

$$\left|S_{quadrature\ hybrid}\right| = \frac{1}{\sqrt{2}} \begin{vmatrix} 0 & S_{12} & S_{13} & 0 \\ S_{12} & 0 & 0 & S_{24} \\ S_{13} & 0 & 0 & S_{34} \\ 0 & S_{24} & S_{34} & 0 \end{vmatrix} \tag{20}$$

It is important to note that S-parameters are defined as normalized voltages and can be converted into normalized power as shown in

$$P_{ij} = |S_{ij}|^2 \tag{21}$$

The goal is to see how the performance of the SIMC varies when different power distributions flow through the quadrature hybrid. S_{12} is the voltage going from port 1 to 2 and is going to be defined as the dependent variable set by the user. Assuming that the quadrature hybrid is lossless, then from (21) and (20)

$$|S_{13}|^2 = 1 - |S_{12}|^2 \tag{22}$$

when substituting the previous equation in the second and third row of (20) it results in

$$|S_{24}|^2 = 1 - |S_{12}|^2 = |S_{13}|^2 \tag{23}$$

$$|S_{34}|^2 = |S_{12}|^2 \tag{24}$$

The new S-parameters are only modified in magnitude. The electrical length between ports remain unchanged at $\lambda/4$ and maintain the same phase difference be-

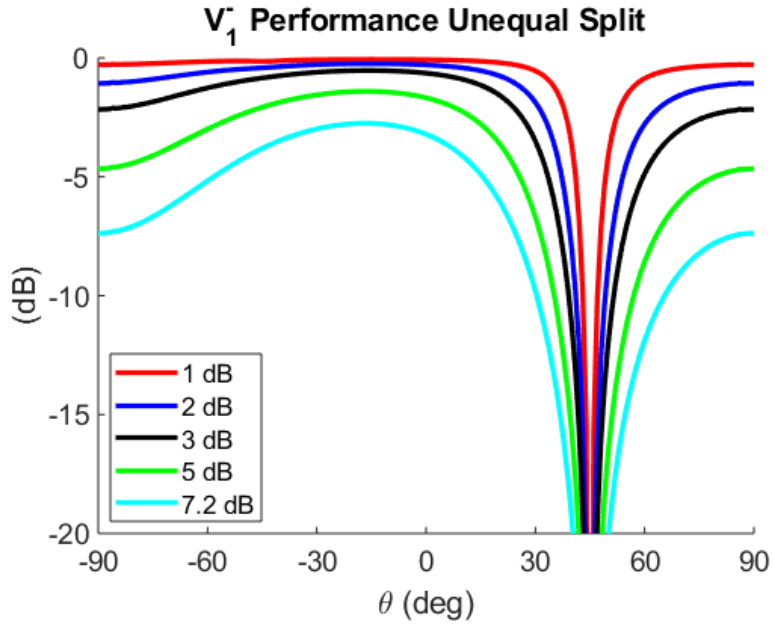

Figure 2.4: Performance of the SIMC when using different unequal split quadrature hybrids.

tween ports as occurs in the equal split design. The new S-parameter values defining the unequal split quadrature hybrid are a function of S_{12} and are theoretically realizable because these new expressions for S_{13}, S_{24} and S_{34} comply with the unitary matrix. Simulations were run when substituting the new S-parameters in the closed-form expression from (15). The results are shown in Figure 2.4. A more selective null and less overall IL is achieved when increasing the ratio of S_{12}/S_{13}.

The results shown in Figure 2.4 are very beneficial because the improvement of the IL of the SIMC is related to the width of the null. Ideally however, they would be independent from each other. Figure 2.5 shows the analysis of the power that flows through the whole system when the null is placed at $45°$. Figure 2.5a shows the power in relation to the angle of incidence when the quadrature hybrid has an equal split ($S_{12} = 3$ dB). A more optimized case is shown in Figure 2.5b for an unequal split quadrature hybrid with $S_{12} = 1$ dB. When the system is in receive mode, a plane wave will excite port 2 (P2) of the quadrature hybrid with a normalized

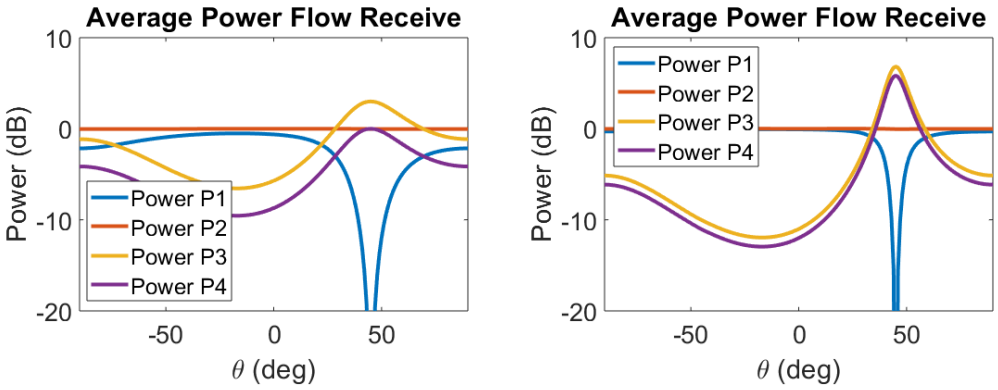

(a) Power Flow Equal Split ($P_{12} = 3$) dB (b) Power Flow Unequal Split ($P_{12} = 1$) dB

Figure 2.5: An illustration of the power flow of the SIMC through each port of the quadrature hybrid related to its angle, where P3 is the power going into the general two-port network.

power of 0 dB after de-embedding the active reflection coefficient. As expected for the pass-angle at $45°$, most of the power will flow directly into port 1 (P1) which is the node connected to the RF front end. The power going into the cancelling feeding path, represented as port 3 (P3) and port 4 (P4), will be minimal for the pass angles. When the incident wave is at the incoming angle of the null placement, the power going into P1 tends to approximate to 0 ($-\infty$ in dB). Since the system is lossless all the power is redirected into the cancelling feeding path, P3 and P4. That means that there is a negative impact when decreasing the IL of the SIMC. That trade-off is shown in Figure 2.5b when the cancelling signal flows with higher power through the general two-port network after increasing $|S_{12}|$. That increase goes from 3 dB for an equal case to 6.8 dB for the $P12 = 1$ dB case, as shown in Figure 2.5. This might be a concern because in order to get real-time null-steerability, the general two-port network will most likely be an active or semi-active component. A higher power flowing through an active component can compromise its linearity, creating harmonics and decreasing the system's dynamic range.

It is mathematically proven that the IL loss can be decreased and the null can be

narrowed, allowing for a lower noise figure and a more efficient scanning volume. When changing the power distribution of the quadrature hybrid, the properties of the general two-port network also need to be changed. From (16) it can be seen that the IL of that two-port network is only a function of the S-parameters of the quadrature hybrid. When (23) and (24) are substituted in (16) and the magnitude is taken, the whole expression can be rewritten as

$$|S_{12a}| = \left| \frac{S_{12}}{S_{12}^2 - S_{13}^2} \right| = \left| \frac{|S_{12}|j}{(|S_{12}|j)^2 - (-|S_{13}|)^2} \right| = |S_{12}| \tag{25}$$

This result shows that the IL of the two-port network needs to be the same as the S_{12} of the quadrature hybrid. The result obtained in (25) will be used to calculate the IL of the two-port network for the following sections. It is also shown that there is a relationship between the IL of the two-port network (or quadrature hybrid) and the spatial response. This type of work has never been done before and there are not any metrics that characterize the performance of spatial nulling. Figure. 2.6 aims to identify overall system performance with respect to the IL of the two-port network S_{12a}. It shows the IL of the SIMC for its optimum angle (left Y-axis, blue line) versus the IL of the two-port network, demonstrating how the SIMC IL improves when reducing S_{12a}. The right Y axis shows the percentage of pass angles that are -3 dB or less with respect to the best angle (the higher the better).

For example, an equal split quadrature hybrid needs to have a two-port network that has an IL of 3 dB. In this case, the best performing scan angle will have an IL of 0.5 dB. The quantity of angles that have a 3 dB IL or less with respect to the IL of the optimum angle amounts to 84.62%.

The impedances of the lines (Z_1 and Z_2) defining the quadrature hybrid shown in Figure. 2.7 can be found using even and odd mode analysis. It is beneficial to calculate the impedances as a function of gain defined as V_{P2}/V_{P3} because the

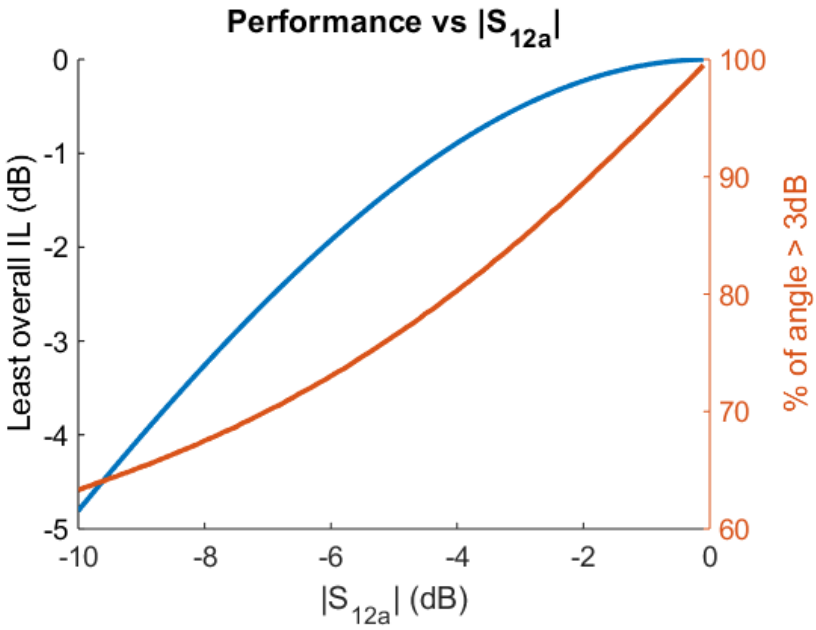

Figure 2.6: Illustration of the SIMC performance versus S_{12a}, comparing the overall IL and the percentage of angles that have less than 3 dB IL with respect to the best performing angle.

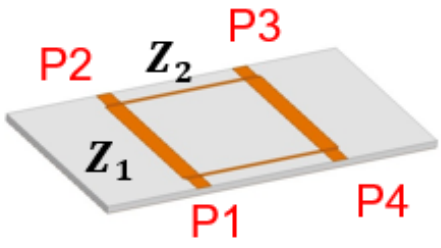

Figure 2.7: Illustration showing the two impedances defining the power distribution of the quadrature hybrid.

result can then be related directly to S_{12} of the quadrature hybrid. Then Z_1 can be expressed as

$$Z1 = \sqrt{\frac{Z_0^2 Z_2^2}{Z_2^2 - Z_0^2}} \tag{26}$$

Z_1 ensures that the quadrature is matched to the characteristic impedance (Z_0) of the system. Z_2 defines the power split between P2 and P3 and it equates to

$$Z2 = Z_0 \sqrt{\frac{G^2}{1 - G^2}} \tag{27}$$

where $G = V_{P2}/V_{P3}$. These line impedances can then be converted into equivalent line widths using "ADS line calc". These derivations are going to be of great importance when the SIMC is calculated and implemented because quadrature hybrids need to be adapted to the IL provided by the general two-port network, as shown in the next sections/chapters. For simplicity, the next section uses equal split quadrature hybrids to verify the mathematical model and its closed-form expression found in (15). A full-wave simulator is used to simulate the SIMC in an infinite array environment and the results are then compared to the mathematical model.

2.3 SIMC Unit Cell Simulated Results

The easiest way to verify that a null was accurately positioned for a certain incoming wave is by using a full-wave electromagnetic simulator (HFSS). An infinite array approach was used in HFSS to verify the results obtained with the mathematical model, because they both use the unit cell representation. A $\lambda/2$ size unit cell was designed, emulating a planar infinite array approach using Floquet ports and master/slave boundaries. The SIMC is designed on a 3D structure with a Rogers 4350B dielectric, chosen because of its low cost and low loss. The thickness of

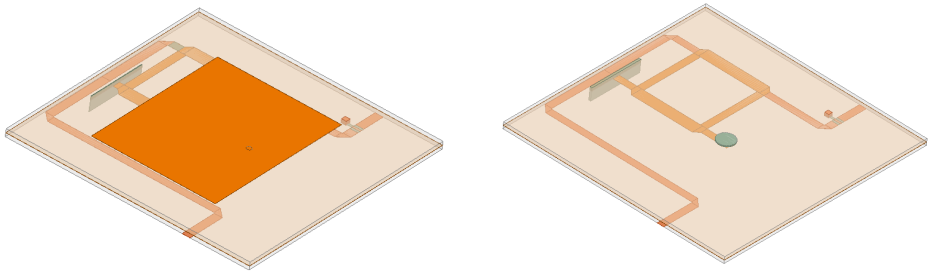

(a) Unit Cell With Patch (b) Unit Cell With Port

Figure 2.8: The microstrip patch antenna of the bottom layer of the unit cell (a) is replaced by a port (b).

the Rogers 4350B dielectric is 30 mils and it operates at 2.75 GHz. The full structure (Figure 2.8) uses three layers; the top layer has the SIMC, the middle layer is composed of a ground plane, and the bottom layer is composed of the radiating element, initially a patch antenna. However, as explained in a previous section, the patch antenna is replaced with a port to simulate the performance of the spatial interference mitigation network independently of the performance of the antenna. These changes are shown in Figure 2.8. The mathematical and simulated results can now be compared, as shown in Figure 2.2, where a close agreement is seen between both models (black trace). This figure shows an achievement of nulls that provide up to 25 dB of mitigation for the simulated results. The mathematical model allows the extraction of optimal attenuation values because it takes into account the loss of the traces, as well as slight imbalances in a real quadrature hybrid. Optimal attenuation values translate into a deeper null. Due to these imperfections, the attenuation that gave the best performance was found to be $S_{12a} = 2.81$ dB instead of the 3 dB of that derived in the ideal case.

The mathematical model accurately predicts the deepness of the null and its placement in the spatial domain, especially when real values of loss and quadrature hybrid imbalances are taken into account. Despite the fact that the mathematical

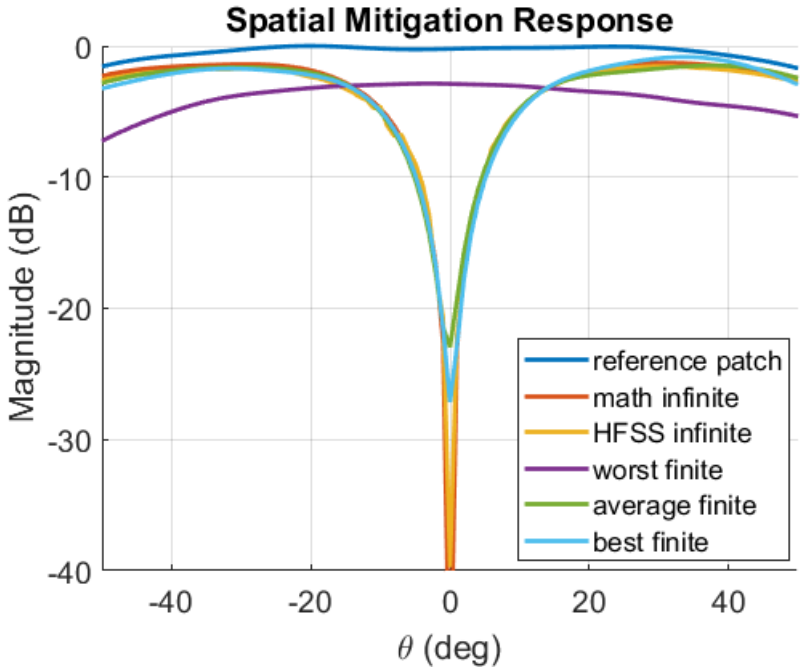

Figure 2.9: Comparison between a patch antenna without the SIMC for the mathematical model of the unit cell, HFSS unit cell and HFSS results for a linear array showing the worst, average, and best performing element of an array with the null scanned to broadside.

model is accurate in a infinite array environment, it is inaccurate predicting the performance of the first elements of the array as seen in Figure 2.9. This reflects the performance of the worst, average, and best finite array responses of a simulated 1x8 array in comparison to the spatial response of the infinite array. The first element of the array will have the worst performance because it does not have the cancelling signal provided by the adjacent element.

The worst performing element will always be the first element of the array because it has no signal from the adjacent element to provide destructive interference for the null or constructive interference for the desired scan angles. After the first element, the cancelling signal starts to increase in amplitude as it progresses through the elements of the array until it approximates the amplitude of the infinite array response. After taking multiple measurements, the 4th or 5th element will show a

spatial response that approximates to the infinite array response. To see the true performance of the SIMC, a more detailed analysis is needed that requires analyzing the embedded element patterns for different angles and comparing the simulated results with measured results in order to determine how much mitigation can be achieved before the interferer enters the receiver chain.

This chapter shows a full theoretical analysis for the SIMC when placed in an infinite array and proves that a steerable null can be placed before the RF front-end. This analysis includes predicting the null depth and placement as well as the IL for the pass angle. This chapter also focuses on optimizing the spatial response by changing the power split of the quadrature hybrid. The next chapter focuses on designing and prototyping a finite linear array of 8 elements for measuring the performance of the SIMC on a real array.

3 SIMC Applied to a 1x8 array

The mathematical model is derived for a unit cell representing an infinite array approach, and when compared to simulated results, close agreement is shown. However, a finite array is needed to prove that this structure works in a real environment where measurements are taken and compared to simulated results. Since the mathematical model and the simulated model closely agree for the infinite array case, a close agreement between measurements and simulated results, for a finite array case, would further validate the mathematical model. With the use of HFSS, the authors concluded that a 1x8 array would be an excellent size array to show the effects of the SIMC, due to low computational resources, while still being big enough for the spatial response to converge towards the results found for the infinite array. Such results enable the comparison between mathematical and simulated results with measurements. The infinite array response is of interest because it serves as the reference of the null's magnitude. The 1x8 array was designed using a full wave electromagnetic solver (HFSS) where the SIMC is on one layer, the antenna at another layer and a ground plane separating those two layers. The dielectric used for the radiating layer is a $125-$mil thick Duroid 5880.

Two types of SIMC structures were simulated, fabricated and measured. The first type of SIMC being the ideal case where an equal split quadrature hybrid is used. In that case, the resulting IL needed of the S_{12a} is 3 dB. Coaxial cables and female-to-male connectors were used to provide null steering. The coaxial cable interconnecting the elements had a measured IL of about 0.8 dB, therefore, a 2 dB attenuator was used (adding to a total value of 2.8 dB, approximately the same as the optimized solution shown in Figure. 2.2). The phase shifting for θ_2 was created by using a coaxial cable and a female-to-male adapter, which add an extra 70° of delay each at 2.75 GHz, replicating a tunable electrical length. Those extra delays

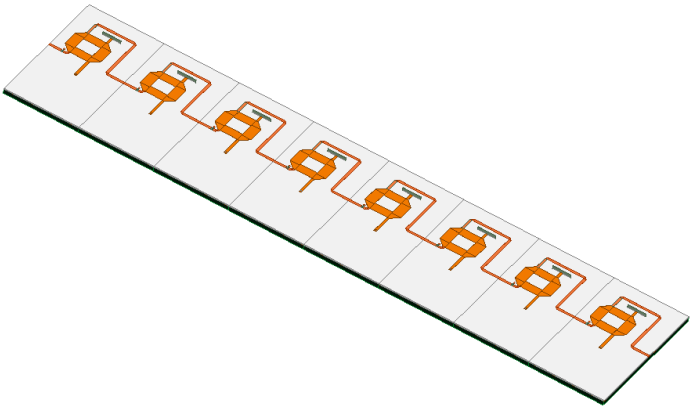

(a) SIMC layer

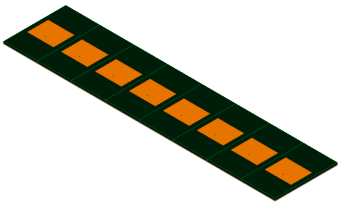

(b) Radiating Layer

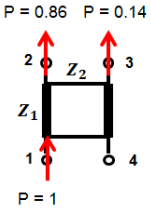

(c) Unequal Split Quadrature Hybrid

Figure 3.1: An illustration of a 1x8 array of patch antennas with (a) SIMC layer interconnecting elements and also probe feeds directly into (b) each patch antenna. (c) unequal quadrature hybrid design.

will change the phase of the cancelling signal feeding into the adjacent element and changes the location of the nulls. Two different null placements where obtained using: none and 1 female-to-male connectors. Knowing the total delay of the line θ_2, the nulls were predicted to occur at $0°$ and $-20°$ according to the mathematical model (15).

The second SIMC was designed to accommodate an electronically steerable null was implemented with phase shifters. Those phase shifters boards were pre-programmed and readily available to the authors of this research. The drawback was that the IL of those phase shifters oscillated between 7.2 and 7.7 dB as a function of angle. That meant that an unequal split quadrature hybrid was designed and fabricated as shown in Figure. 3.1. The unequal power split was designed con-

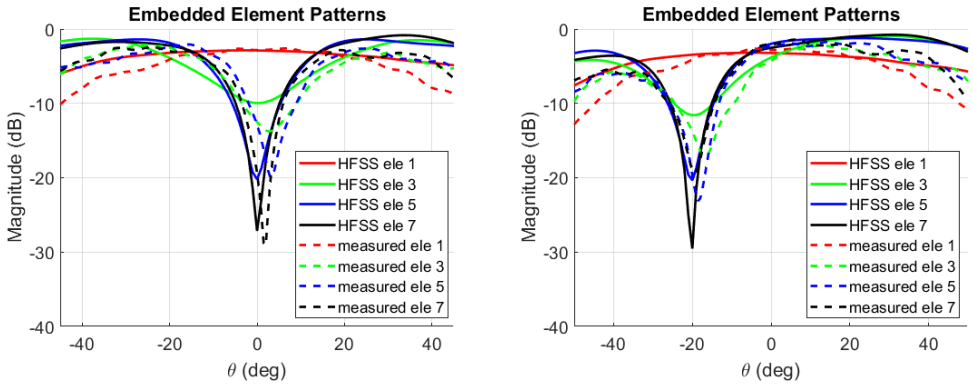

(a) null placed at $0°$ (b) null placed at $-20°$

Figure 3.2: Measured vs simulated embedded element pattern for the equal split quadrature hybrid case two different null placements.

sequently with the results obtained from (15) to compensate for the high IL. The consequence was an increase of the overall IL of the system; however, it served as a proof of concept for electronic null steering. In order to achieve the unequal power split, the impedances of the line had to change to $Z_1 = 18.79\Omega$ and $Z_2 = 20.28\Omega$ (Figure. 3.1c).

3.1 1x8 Embedded Element Pattern Measurements

The SIMC spatial performance using the equal split quadrature hybrid is shown in Figure. 3.2 and illustrates measured vs simulated embedded element patterns for the 1,3,5 and 7th element of the 1x8 array with nulls at $0°$ and $-20°$. As previously discussed, the first element has bad performance, but the other elements have an IL of less than 2 dB (considering that the roll-off of the antenna pattern is embedded in the result too). Nulls of 15 dB are usually achieved after the 4th element.

Similar results are shown in Figure. 3.6 where, as expected, a higher IL due to the unequal power splits is reflected on the embedded element patterns. At best, an IL of 5 dB is achieved; however, deep nulls of more than 15 dB were measured. In this particular case, the 7th element was performing better than the 8th, possibly do

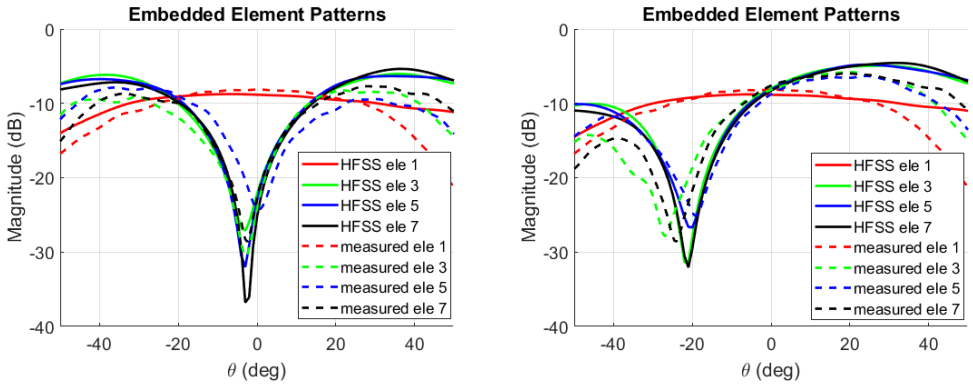

(a) null placed at 0°

(b) null placed at 20°

Figure 3.3: Measured vs simulated embedded element pattern for the unequal split quadrature hybrid case (with phase shifters) two different null placements.

to the errors provided by the discrete values of the digital phase shifter. For both cases, the equal split and phase shifter case, the performance of the SIMC decayes as the nulling is placed away from broadside.

To fully measure the IL and spatial mitigation provided by SIMC, analog beamforming (ABF) was done for both cases again, with the nulls placed at broadside and away from broadside to calculate the IL and the effective spatial mitigation. These measurements were compared to measurements done with just the array, without the structure. The measured IL of the equal split power divider was 1.16 dB, and a spatial mitigation of 13.88 dB, therefore having an effective mitigation of 12.72 dB at the array level, that is including the first element. For the case where phase shifters were used, an IL of 5.34 dB was measured with a spatial mitigation at broadside of 20.64 dB resulting in an effective mitigation of 15.3 dB.

After the nulls in the embedded element pattern were well determined, allowing to spatially mitigate an interferer by providing a notch in the desired direction a new case 'real scenario' demonstration is explained in the next section where an interferer is mitigated before it enters the receiver and preventing it from compressing the first component of the receiver.

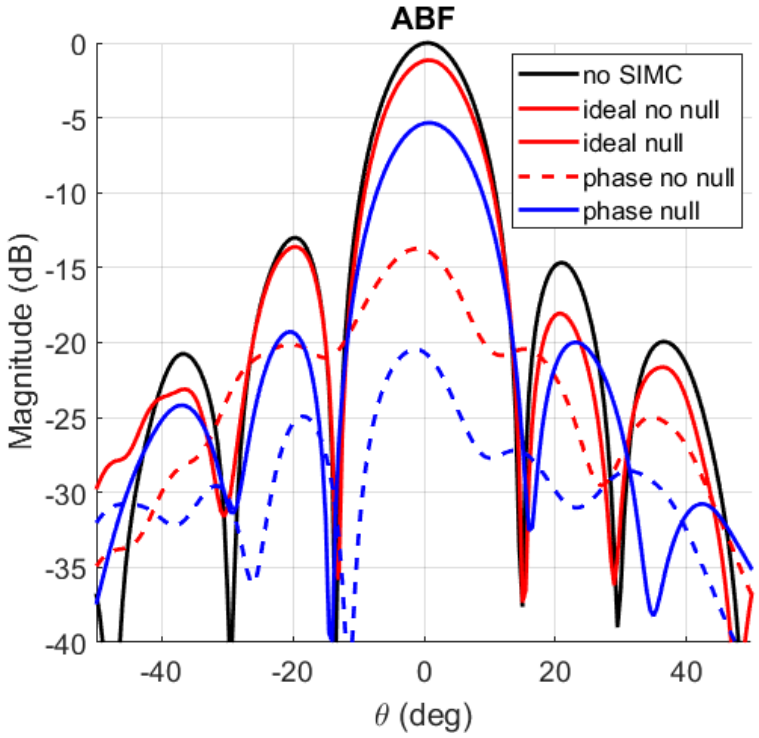

Figure 3.4: Measured ABF at broadside to determine IL and SIMC performance at array level.

3.2 1x8 Array System Level Demonstration

The goal is to reduce the necessary dynamic range of the components in the receiver chain by mitigating potential strong interferers at the RF frontend. After verifying, using an anechoic chamber, that each embedded element pattern is able to steer a null towards the interferer with depths of more than 15 dB for different angles, a real case scenario was presented. An interferer blinds with an incoming angle of $-20°$ blinds the desired signal at broadside by driving the LNA into compression.

The array was situated as shown in Figure. 3.5, where there was a desired $5MSPS$ QPSK signal at broadside in the presence of a stronger CW interferer. The interfering signal was strong enough to compress an off-the-shelf LNA connected to the final element as shown in the top left plot. This resulted in an intermodulation

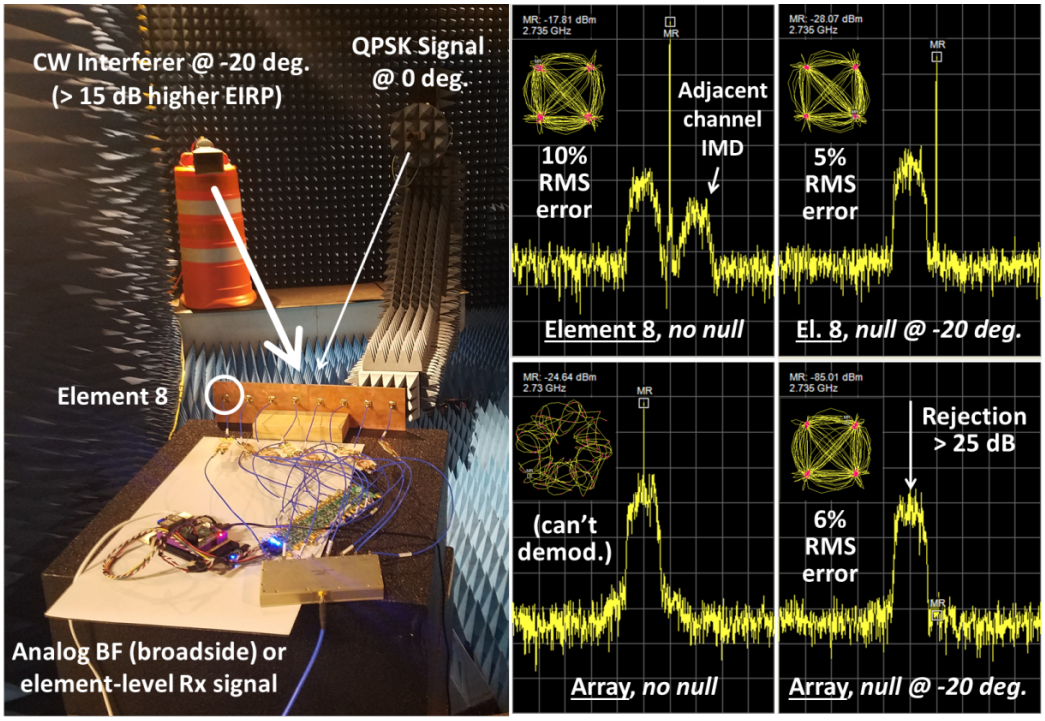

Figure 3.5: (Left) Setup for system-level demonstration of array-level interference rejection; (top right pair) resulting spectra and constellation diagram for a single element, as would be relevant for a digital array, clearly showing effects of IMD and compression; (bottom right pair) corresponding results for an ABF array steered to broadside, with an interferer on top of the signal, showing depth of array-level notch just prior to compression.

distorsion (IMD) and loss in SNR. After steering the null, the interferer was mitigated more than 10 dB. The real mitigation is higher because the IL of the SIMC at 20° and going from compression to the LNA's linear region is included in those 10 dB. Therefore, it can be concluded that the total mitigation is similar to the values obtained when measuring the embedded element patterns.

To investigate the null depth at the array level, the same experiment was repeated but now all elements were power combined, effectively beamforming at broadside towards the signal of interest. The interferer is now leaking through the first sidelobe (at -20°) and clearly preventing the receiver to demodulate. After steering the null towards the interferer, more than 20 dB of mitigation was achieved and the

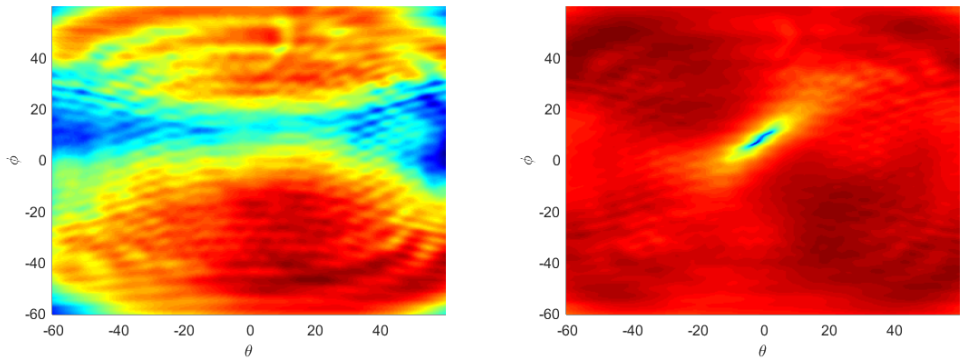

(a) null cuts the whole plane (b) null

Figure 3.6: An illustration (a) on how the current circuitry performs for all θ, ϕ angles and (b) an illustration of the desired spatial response for the same angles.

signal was successfully demodulated.

These results prove that the SIMC works in a real case scenario when the interferer is successfully mitigated. However, there are two basic things that need to be addressed here. One is that the analysis up until this point is done in just one plane where the incoming angle was a function of θ. Figure. 3.6a shows the measured nulled embedded element pattern in ϕ, θ, and as shown in the picture, a null is created for $\phi = 10°$. With the current circuitry, all angles for θ are nulled when $\phi = 10°$, depending on how the array is positioned. The power of the signal for all angles on the nulled plane is reduced, mitigating the interferer, but also other possible targets, therefore reducing the sensitivity of the receiver for that angle. Since interferers are usually a point in space, a pinpoint null is the most desirable spatial response to maximize the interferer-free scanning volume. An example of a pin-point null is illustrated in Figure. 3.6b where it is placed for $(\theta, \phi) = (10, 10)$. Chapter 4 solves this problem by creating a cancelling signal that is a function of two-dimensions and thus requires a planar array.

Another way to improve the interferer-free scanning volume is to decrease the size of the null. As shown in this chapter, the IL is less than 1 dB for the equal

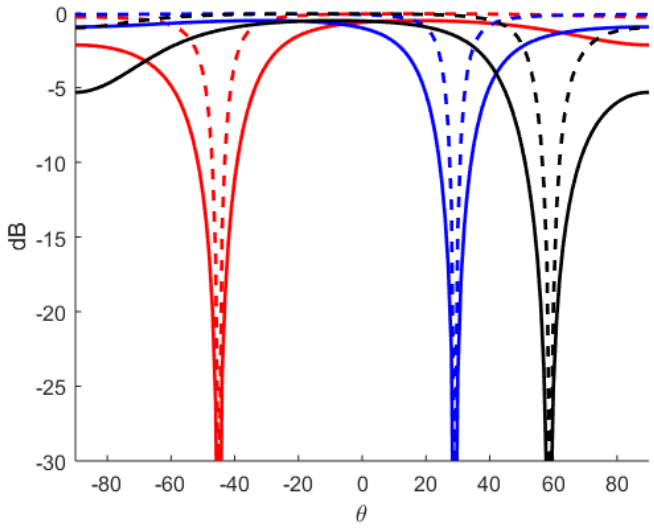

Figure 3.7: An illustration of SIMC's efficiency when changing the power flow of the quadrature hybrid, where the solid line shows the spatial response for an equal power distribution and the dashed lines it for an unequal split where more power in the same branch.

split quadrature hybrid case for most angles outside of the null. However, in order to reduce the noise floor and increase receiver sensitivity, it would be desirable to reduce the IL even further. In this chapter it is shown that phase shifters with 7 dB of IL are not a good option to create steerable nulls. In general, phase shifters have high IL and are costly. The goal in Chapter 5 is to show ways to address all negative factors that arise when the phase shifter is substituted with a tunable filter. To show the resulting improvements, the optimized SIMC is implemented in a linear 10 element array.

4 Two Dimensional SIMC for Planar Arrays

In previous chapters a circuitry capable of creating a null in one dimension is demonstrated (defined as θ), but when the embedded element pattern is viewed in 3D (θ, ϕ), the null cuts the entire plane. The technique of placing a null to provide a cut in the entire angular plane (θ or ϕ) before the RF front-end is usually not desired, because in the same plane, all information in addition to the interferer, is mitigated. In such a case, if there is an SoI in the plane, it will be mitigated and can possibly fall under the noise floor if the signal is weak enough. In order to maximize the effective scanning volume, a pinpoint null, also called a two-dimensional null, is desired. The goal is to locate a two-dimensional null in the spatial response before the signal enters the receiver. For illustration purposes, a null is placed at approximately $(\theta, \phi) = (45, 30)$ in Figure 4.1.

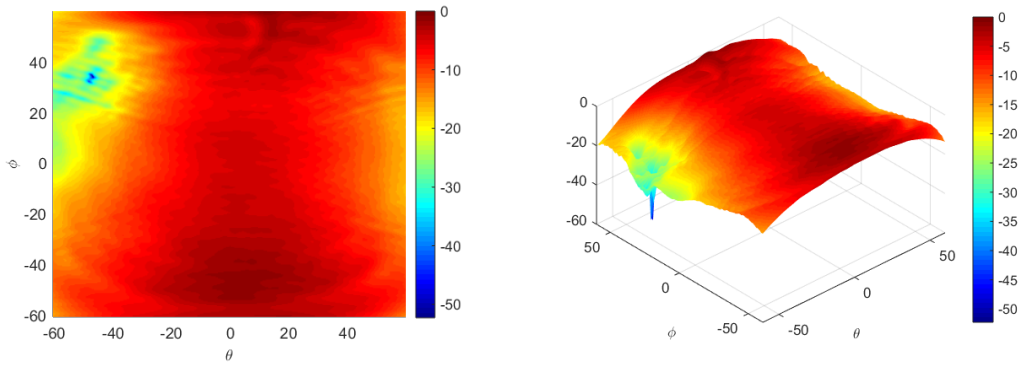

(a) 2D view of the nulled embedded element pattern

(b) 3D view of the nulled embedded element pattern

Figure 4.1: Illustration of the spatial response of the normalized gain of the embedded element pattern when viewed in (a) 2D and (b) when viewed in 3D.

The author would like to clarify that in previous chapters, θ was defined as the angle of incidence of the plane wave and ϕ was defined as the progressive phase shift, a notation commonly used for linear arrays. However, in this chapter, θ and ϕ are defined as elevation and azimuth angle respectively. The progressive phase

shift in the X dimension is defined as α and as β for the Y dimension, as shown in Figure 4.2.

The theory in previous chapters was based upon using one adjacent element to feed the cancelling signal into the next cell, thus providing a null in one direction. For pinpoint nulling the destructive interference introduced needs to have the phase information for the vertical and horizontal phase shifts. To obtain the required phase shift, a cancelling signal that is a combination of the elements from the same row and same column as the element that has a null in the embedded element pattern. must be fed to the 2D spatial interference mitigation circuitry (2DSIMC). This schematic is shown in Figure 4.3

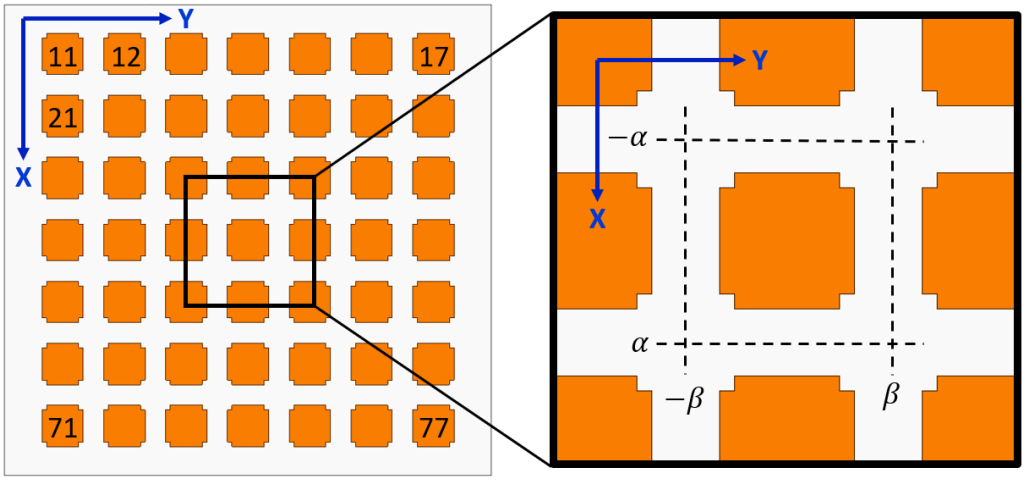

Figure 4.2: An illustration of an equivalent unit cell on the right that was extracted from the 'large' array on the left.

As shown in Figure 4.3, the new circuitry combines the progressive phase shifts coming from adjacent elements in both the vertical and horizontal directions. These signals with the progressive phase shifts added are fed into a power combiner that results in a summed signal possessing two phase shifts, one for each dimension. This signal is then fed into the quadrature hybrid to provide the destructive interference needed to create a null in the desired direction. This technique is aimed to

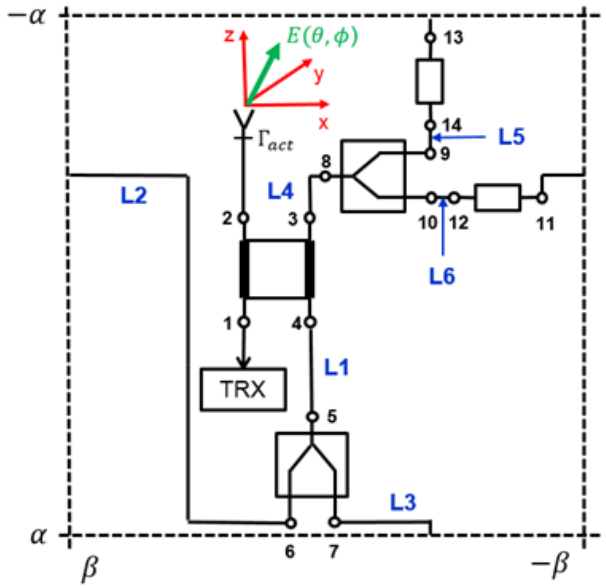

Figure 4.3: A circuit schematic of the 2DSIMC layer.

be used in large arrays, therefore the infinite array approach is used to model this circuitry and Floquet theory and its boundary conditions are applied in the same way as in previous chapters. Floquet theory assumes that there are infinite radiating elements that each have the same properties, therefore the modelling can be simplified by analyzing a single element placed in an infinite array called a unit cell. This theory assumes that all embedded element patterns are the same and the edge effects are neglected, thus allowing a simplified mathematical model. The mutual coupling for infinite arrays is embedded as the active reflection coefficient and is equal for each element. Each boundary is defined with a progressive phase shift. The progressive phase shifts are defined in two dimensions, α for the vertical dimension or Y axis, and β for the horizontal dimension. It might seem obvious, but it is still worth mentioning that the β from Figure 4.2 and Figure 4.3 are mirrored. This mirroring occurs because the 2DSIMC is placed in the back of the array, but when both sides are visualized from the top, one appears flipped from the other in the Y axis.

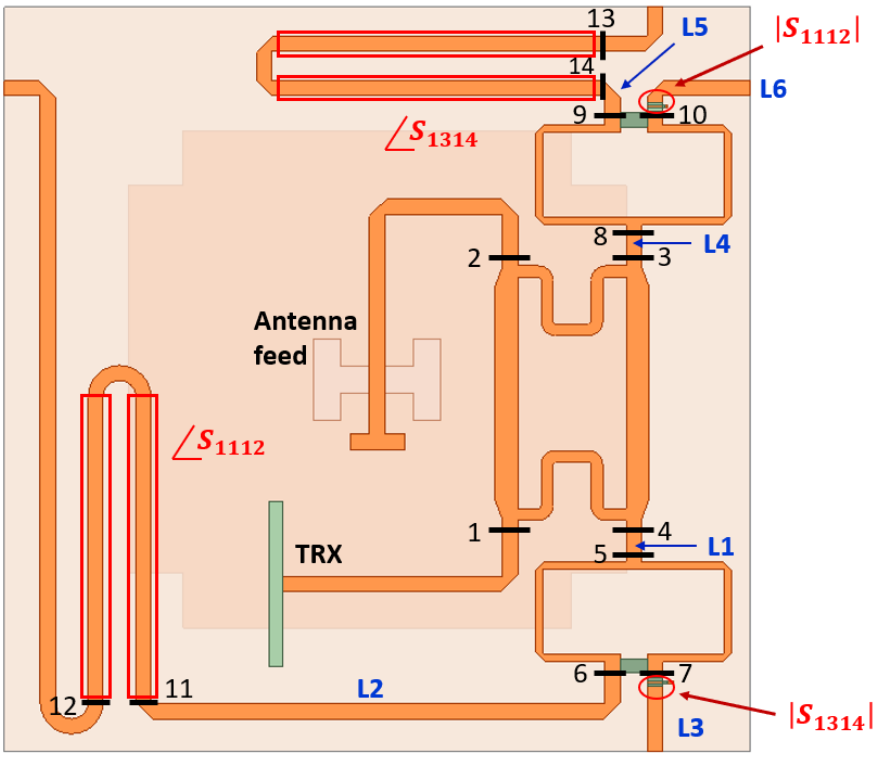

Figure 4.4: The equivalent layout of the circuit schematic unit cell represented in Figure 4.3.

4.1 2DSIMC Mathematical Modelling for a Unit Cell

The goal for obtaining a 2D null is to derive an expression that quantifies the voltage going into the receiver for a certain scan angle $V_1^-(\theta, \phi)$, and to explore the possibility for V_1^- to be a function of other tunable components. S-parameters are used for the analytical modelling. The scattering matrix for the quadrature hybrid is the same as the one used in chapter 2 where

$$\left|S_{quadrature\ hybrid}\right| = \frac{1}{\sqrt{2}} \begin{vmatrix} 0 & -j & -1 & 0 \\ -j & 0 & 0 & -1 \\ -1 & 0 & 0 & -j \\ 0 & -1 & -j & 0 \end{vmatrix} \tag{28}$$

The two Wilkinson power dividers shown in Figure 4.3 are identical and defined as

$$\left|S_{quadrature\ hybrid}\right| = \frac{1}{\sqrt{(2)}} \begin{vmatrix} 0 & -j & -j \\ -j & 0 & 0 \\ -j & 0 & 0 \end{vmatrix} \tag{29}$$

Since there are two signals that must be combined two-port networks are needed, one between nodes 11 and 12, and the other between nodes 13 and 14. The two-port networks will manipulate the cancelling signal in amplitude and phase to provide the null for the desired angle. Their expression is

$$\left|P_{1112}\right| = \begin{vmatrix} S_{1111} & S_{1112} \\ S_{1211} & S_{1212} \end{vmatrix} \tag{30}$$

$$\left|P_{1314}\right| = \begin{vmatrix} S_{1313} & S_{1314} \\ S_{1413} & S_{1414} \end{vmatrix} \tag{31}$$

It is assumed that the two-port networks are perfectly matched and there will not be any reflections, thus: $S_{1111} = S_{1212} = S_{1313} = S_{1414} = 0$. The voltage going into the receiver (V_1^-) is found in one of the equations defining the quadrature hybrid (28):

$$V_1^- = V_2^+ S_{12} + V_3^+ S_{13} \tag{32}$$

Where V_3^+ equals to the voltage going out of the Wilkinson power divider V_8^- with

a delay due to L4

$$V_3^+ = V_8^- e^{-jL_4} \tag{33}$$

From (29)

$$V_8^- = V_9^+ S_{89} + V_{10}^+ S_{810} \tag{34}$$

When combining (34) with (33), and the result of that combination is put in (32), the following expression is obtained

$$V_1^- = v_2^+ S_{12} + (s_{89} + V_9^+ S_{810} V_{10}^+) e^{-jL_4} S_{13} \tag{35}$$

That leaves the expression as a function of V_9^+ and $V_1 0^+$, which are the inputs from the adjacent elements that combine inside the power divider. The signal that goes into the power divider is the same one that leaves port 14, therefore:

$$V_9^+ = v_{14}^- e^{-jL_5} = S_{1413} V_{13}^+ e^{-jL_5} \tag{36}$$

V_{13}^+ contains the signal fed from the output of the power divider of the adjacent top element. Since the unit cell is analyzed and all the infinite elements are supposed to have the same properties, Floquet theory determines that the signal is the same as it would be from its own cell except for an added progressive phase shift. In addition to the phase shift, there is a delay created due to L3, resulting in

$$V_9^+ = S_{1413} V_7^- e^{-j\alpha} e^{-jL_3} e^{-jL_5} \tag{37}$$

From the S-parameter matrix off the Wilkinson power divider (29) it is known that

$$V_7^- = S_{75}V_5^+ \tag{38}$$

where V_5^+ is fed by the output of port 4 of the quadrature hybrid V_4^- and has an extra added delay due to L_1, resulting in

$$V_4^- = V_2^+ S_{42} + v_3^+ S_{43} \tag{39}$$

When combining (38) with (33) in (39) and the delay L_1, the following expression is obtained

$$V_9^+ = S_{1413}(V_2^+ S_{42} + V_8^- e^{-jL4} S_{43}) e^{-jL_1} S_{75} e^{-j\alpha} e^{-jL_3} e^{-jL_5} \tag{40}$$

where V_8^- is the output voltage of the power divider combining signals from port 9 and port 10 as shown in (34). This leads to:

$$V_9^+ = S_{1413}(V_2^+ S_{42} + (S_{89}V_9^+ S_{810}V_{10}^+) e^{-jL4} S_{43}) e^{-jL_1} S_{75} e^{-j\alpha} e^{-jL_3} e^{-jL_5} \tag{41}$$

where $V_2^+ = 1$. This assumption can be made because in a large array, each cell has the same excitation in magnitude for each angle, and for simplicity it is normalized to 1. Equation (41) can be reorganized as:

$$V_9^+ = \frac{A + CV_{10}^+}{1 - B} \tag{42}$$

where

$$A = S_{1413} S_{42} S_{75} e^{-j(L_1 + L_3 + L_5)} e^{-j\alpha} \tag{43}$$

$$B = S_{1413}S_{89}S_{43}S_{75}e^{-j(L_1+L_3+L_5)}e^{-jL_4}e^{-j\alpha} \tag{44}$$

$$C = S_{1413}S_{810}S_{43}S_{75}e^{-j(L_1+L_3+L_5)}e^{-jL_4}e^{-j\alpha} \tag{45}$$

From (42) it can be seen that V_9^+, is dependent on V_{10}^+, and models the signal that links the vertical dimensions. V_{10}^+ will provide the solution to the modelling of the signal for its horizontal dimensions. The derivation of V_{10}^+ is similar to the one followed to obtain V_9^+, so the derivation here is going to be covered with less detail. V_{10}^+ can be defined as

$$V_{10}^+ = V_{12}^- e^{-jL_6} \tag{46}$$

It is known from (7) that

$$V_{12}^- = S_{1211}V_{11}^+ \tag{47}$$

when using the Floquet boundary V_{11}^+ equals to

$$V_{11}^+ = V_6^- e^{-jL_2}e^{-j\beta} \tag{48}$$

From the S-parameter matrix of the Wilkison power divider (29) it is found that

$$V_6^- = v_5^+ S_{75} \tag{49}$$

Assuming that $V_2^+ = 1$ V (for the same reason as previously explained) when combining (49), (48), (47) and (46) the resulting expression can be extracted

$$V_{10}^+ = \frac{X + YV_9^+}{1 - Z} \tag{50}$$

where

$$X = S_{1211}S_{42}S_{65}e^{-j(L_1+L_2+L_6}e^{-j\beta} \tag{51}$$

$$Y = S_{1211}S_{89}S_{43}S_{65}e^{-j(L_1+L_2+L_6}e^{-j\beta}e^{-jL_4} \tag{52}$$

$$Z = S_{1211}S_{810}S_{43}S_{65}e^{-j(L_1+L_2+L_6}e^{-j\beta}e^{-jL_4} \tag{53}$$

V_9^+ from (42) and V_{10}^+ from (50) are a function of each other and can be solved as two equations and two unknowns resulting in

$$V_9^+ = \frac{A - AZ + CX}{1 - Z - B + ZB - CY} \tag{54}$$

$$V_{10}^+ = \frac{X - BX + YA}{1 - Z - B + ZB - CY} \tag{55}$$

Referring back to (35), which is the formula describing the voltage going into the receiver, the variables V_9^+ and V_{10}^+ initially were defined as two unknowns. Those unknowns are now substituted with (54) and (55) resulting in the following rather complex expression

$$\begin{aligned} V_1^- = S_{12} + \Bigg[S_{89}\frac{A - AZ + CX}{1 - Z - B + ZB - CY} + \\ + S_{810}\frac{X - BX + YA}{1 - Z - B + ZB - CY} \Bigg] e^{-jL_4} S_{13} \end{aligned} \tag{56}$$

This mathematical expression is derived to maintain its general form so that it allows for the use of any type of quadrature hybrid and power dividers. Finding a

closed-form expression for S_{1312} and S_{1413} is cumbersome. Instead, the procedure that this work uses is based on a numerical approach to find the parameters needed to obtain the null at a specified scan angle. Everything except S_{1211} and S_{1413} must be defined, including parameters such as the lengths of lines, the S-parameters of the quadrature hybrid and power dividers, and the location of the null defined by (θ,ϕ). The angles (θ,ϕ) can be translated into progressive phase shifts as shown in

$$\beta = kd\cos(\phi)sin(\theta) \tag{57}$$

$$\alpha = kd\sin(\phi)sin(\theta) \tag{58}$$

When the distance between elements is $\lambda/2$, as it is in this research, the preceding expressions can be reduced to

$$\beta = \pi\cos(\phi)sin(\theta) \tag{59}$$

and

$$\alpha = \pi\sin(\phi)sin(\theta) \tag{60}$$

Once the correct progressive phase shift between elements is set, the only variables left to determine are S_{1211} and S_{1413}. In this research the correct gains and phase shifts are determined numerically by trying all possible combinations of S_{1211} and S_{1413} to obtain the pair that makes $V_1^+ = 0$ for a specific scan angle. The equation used for the IL of the two-port network is the same as the one found in chapter 2. For an equal split power divider, the IL of S_{1211} and S_{1413} needs to be 3 dB. Once the magnitude is set, the phase needs to be determined. The added phase delay to provide cancellation has to be in the range of 0 and 2π. S_{1211} and S_{1413} can be

visually determined by looking where the V_1^- approximates to zero. The best way to show this concept is to illustrate it with an example. Assuming that some random lengths have been used for $(L_1, ..., L_6)$ and ideal S-parameters of a power divider and quadrature hybrid are used, (28), (29) the following 3D plot can be obtained when a null is needed at a random angle, for example, $(\theta, \phi) = (23, 32)$.

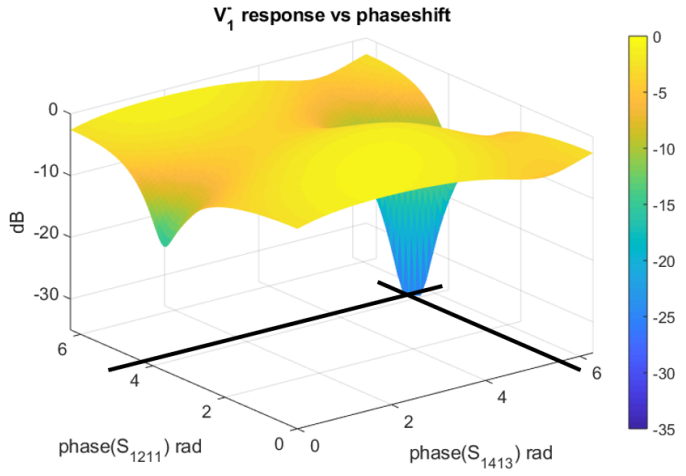

Figure 4.5: Illustration of an example of how the phase of S_{1211} and S_{1413} is found numerically.

From Figure 4.5 it can be seen that the phase that makes the V_1^- approximate to zero occurs when S_{1211} has a phase delay of 4.1 rad and S_{1413} of 5.75 rad.

Figure 4.6 shows the spatial response of the signal going into the RF front end (V_1^-) after finding the lengths of line that define the phase shift from both two-port networks in Figure 4.5. Since it is an ideal mathematical model, the null would be "infinitely" deep in the dB scale and finite when real components are used.

The mathematical model of the signal going into the receiver is now defined. It is demonstrated that the 2D null can be steered by simply changing two phases. Comparing the results of this section to HFSS would further validate the spatial response obtained with the mathematical model.

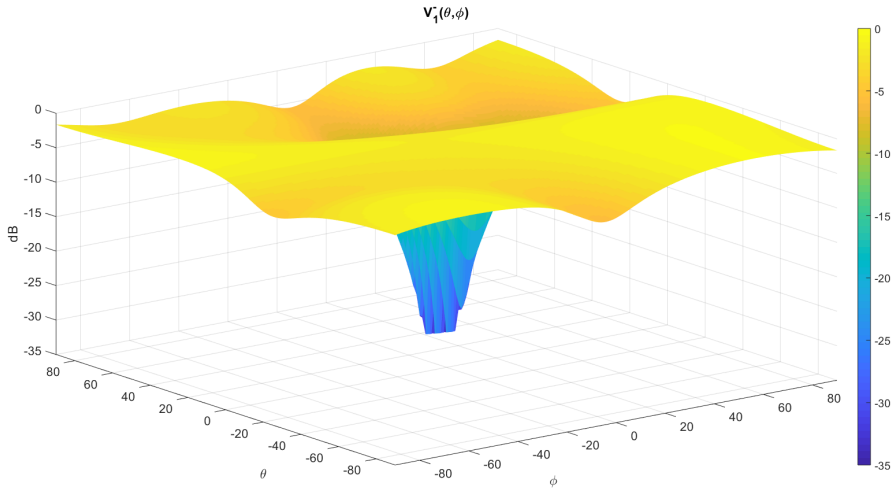

Figure 4.6: Illustration of the spatial response of the 2DSIMC when the null is placed at $(\theta, \phi) = (23, 32)$.

4.2 Unit Cell Design and Layout

The preceding analytical model derived for the 2DSIMC delivers promising results that demonstrate, in theory, that it is possible to have a pinpoint null for a certain angle that can be introduced before the RF front-end that results in maximizing the interferer-free scanning volume. In order to confirm the results of the analytical model, simulations are needed to make sure the 2DSIMC structure behaves the same way as the mathematical model predicts.

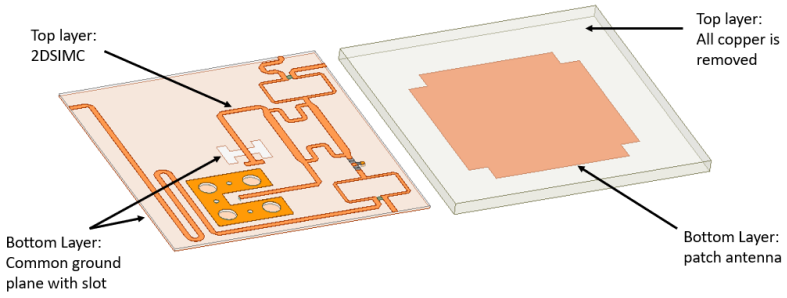

Figure 4.7: Illustration of all layers of the 3D structure: the 2DSIMC, the ground plane with the slot, and the patch antenna.

The radiating element used is an aperture coupled antenna that is re-optimized for a center frequency of 5.5 GHz and built on a 50 mil thick Rogers 5880 LZ substrate. The reason for using this type of patch antenna is because it is easier to fabricate and integrate into the proposed structure, and can be built in-house without having to use multi-layer technology. Figure 4.8 shows how the 2DSIMC and the antenna layer are connected with a slot in the ground-plane that enables transmission between the the top layer and the patch antenna. As previously mentioned, Rogers 5880 LZ is the dielectric used for the radiating layer because it offers a low dielectric constant and increases the bandwidth of the system. The importance of increasing the bandwidth is to eliminate possible errors translated into the spatial response due to a narrow-band frequency response. The ground plane with the slot is on the bottom layer of the 2DSIMC, but that same ground-plane is shared with the antenna layer. The ground plane is sandwiched between the 2DSIMC and the antenna, and nylon screws are used to provide the structural support. The dielectric substrate used for the 2DSIMC is a Rogers 4350B with a 10 mil thickness. This substrate was chosen because it has low loss and high commercial availability. The 10 mil thickness was used to optimize space and allow for thinner transmission lines while still being structurally durable.

The equivalent layout of the circuit schematic from Figure 4.3 is shown in Figure 4.4. Fitting all the components needed on the 2DSIMC layer can be a challenge because the unit cell needs the input to the receiver (an SMA connector for this case), the antenna feed, a quadrature hybrid, and two Wilkinson power dividers. All the RF components need to fit into a $\lambda/2$ sized square. As mentioned before, to steer the null in the desired direction, $\angle S_{1112}$ and $\angle S_{1314}$ need to be specifically set. In previous chapters it was proven that a tunable circuit such as a phase shifter is able to successfully manipulate the null placement. Based on the knowledge

that the null can be electronically steered while simultaneously increasing the circuit complexity in the 2DSIMC, the authors use variable length transmission lines to change $\angle S_{1211}$ and $\angle S_{1413}$. $|S_{1211}|$ and $|S_{1413}|$ are fixed using a 3 dB attenuator (YAT-3+).

The design also needs to take into account that $\angle S_{1112}$ and $\angle S_{1314}$ need to be able to sweep for the full $360°$ of phase shift and locate the null at any desired angle. The equivalent $|S_{1112}|$ and $|S_{1314}|$ are defined by an attenuation of 3 dB and a phase of the delay provided by the equivalent length of the lines. When designing the final layout of the board it was observed that instead of two attenuators, only one was needed if it was strategically placed as shown in Figure 4.8. This improvement supposes a reduction in cost and soldering time.

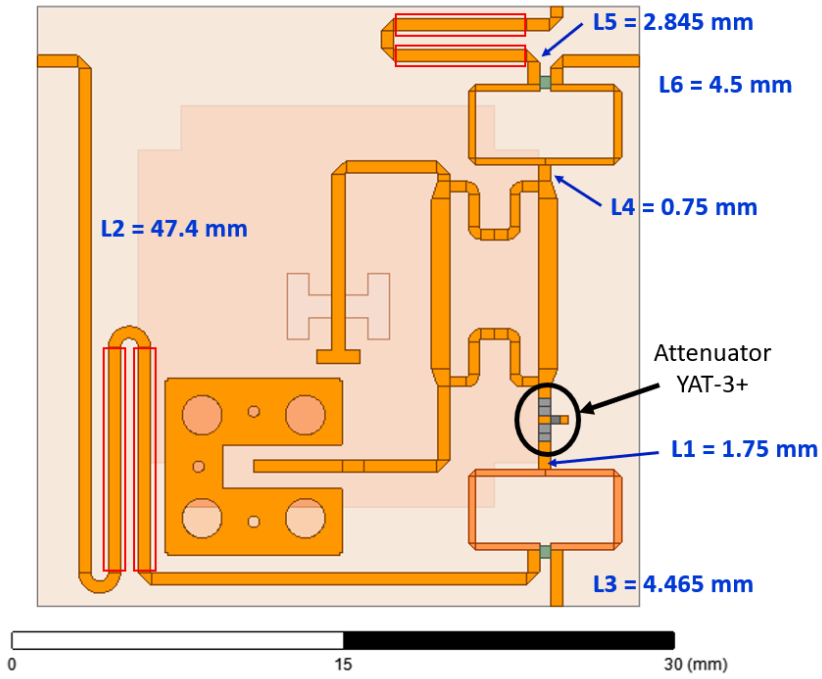

Figure 4.8: The unit cell final layout.

The $L_1, ..., L_6$ that form expression (56) are shown in Figure 4.8 and they include all the lengths of lines with exception of those used in the passive components

themselves: the two power dividers, the folded quadrature hybrid, and the attenuator (in the black circle). The length of lines in Figure 4.8, those that are marked inside of the red rectangle, are not included since those must be variable to facilitate the null placement and provide the phase shift calculated for $\angle S_{1112}$ and $\angle S_{1314}$. The equivalent lengths are converted into electrical lengths by using

$$L_n(rad) = 2\pi L_n/\lambda_{eff} \tag{61}$$

where

$$\lambda_{eff} = \frac{c}{f_{op}\sqrt{\epsilon_r}} \tag{62}$$

The next objective was to find an attenuator that was as close as possible to 3 dB IL at the operating frequency and possessed a small footprint. The attenuator chosen was a Minicircuits YAT-3+ which has 3.2 dB IL at 5.5 GHz and a total surface area of just 2 x 2 mm (Figure 4.9a).

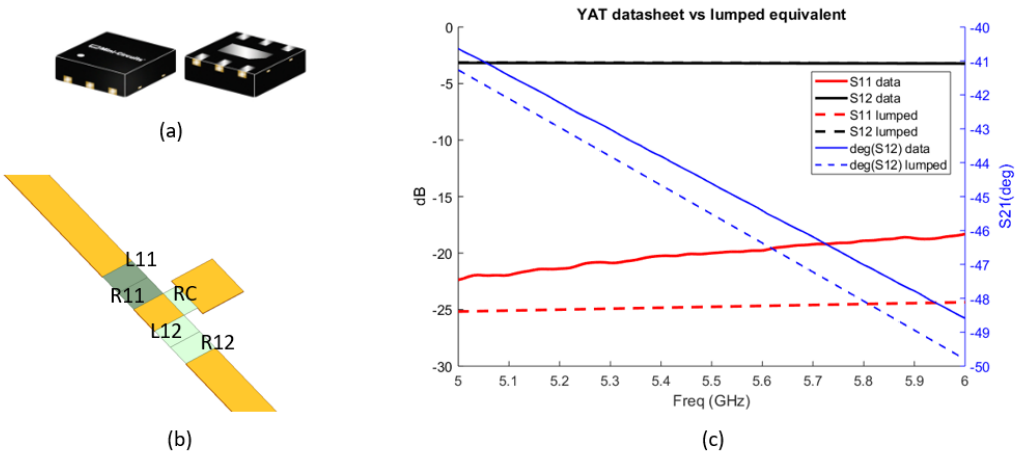

Figure 4.9: An illustration of (a) the attenuator used for 2DSIMC (b) HFSS equivalent lumped element T-network and (c) the S-parameters of the data sheet compared to the simulated lumped element T-network designed for this research.

The S-parameters provided in the data sheet of the YAT are shown with solid lines in Figure 4.9c. Since HFSS is a numerical 3D solver, it does not allow for including objects that are defined with S-parameters. HFSS can interconnect objects using Ansoft Designer that is provided in the ANSYS software package. However, instead of complicating the 3D computer simulation model, it was decided that it was better to use an equivalent lumped network that would provide the same IL and phase shift in the transmission line as is used in YAT-3+. A T-network was designed and simulated in HFSS as illustrated in Figure 4.9b. The S-parameters of the T-network and the YAT-3+ are compared in Figure 4.9. The results show that the T-network IL matches very closely, but the phase difference is 1.1° at 5.5 GHz. Finally the values used are $L11 = L12 = 0.2743$ nH, $R11 = R12 = 8.893\Omega$. The RC has a resistance of 152.66Ω and a capacitance of 0.23 pF in parallel.

For the power combiner, an "almost" equal split Wilkinson power divider was designed, with a reasonable $>$ 20 dB isolation between ports 2 and 3, as shown in Figure 4.11b. The slight imbalance of the power split perfectly accommodates the higher IL of the YAT-3+. All ports have good impedance matching with 20 dB reflections or better.

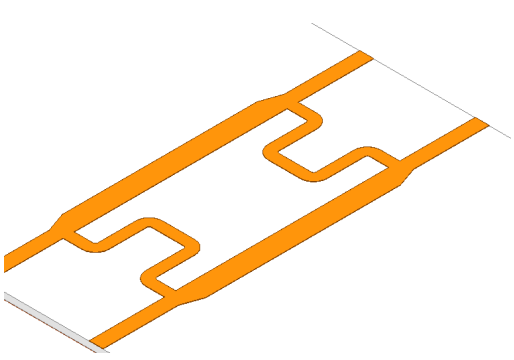

(a) S-parameters of the power divider

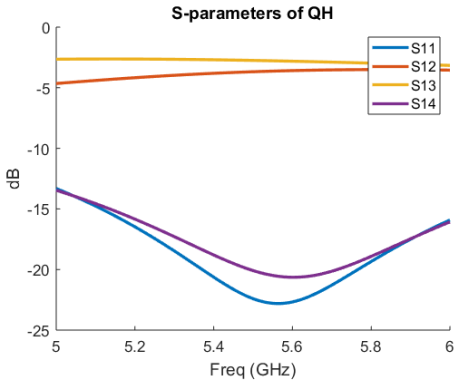

(b) S-parameters of the quadrature hybrid

Figure 4.10: HFSS results of the designs of (a) power divider and (b) quadrature hybrid that are later used for the mathematical model and final fabrication layout.

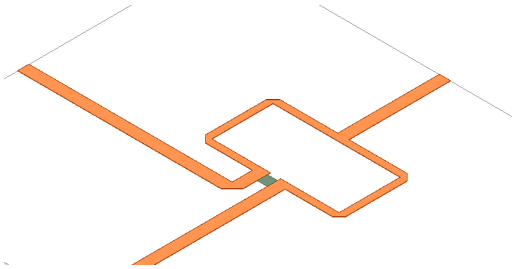

(a) S-parameters of the power divider

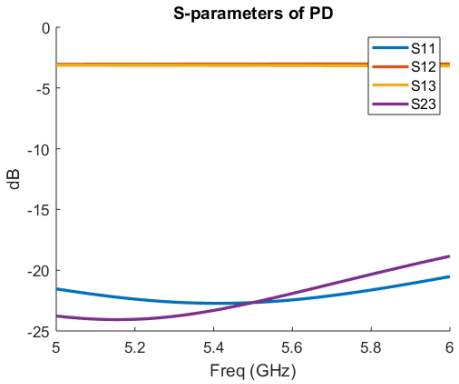

(b) S-parameters of the Quadrature Hybrid

Figure 4.11: HFSS results of the designs of (a) Power divider and (b) Quadrature Hybrid that are later used for the mathematical model and final fabrication layout.

From chapter 2 it is known that the power split of the quadrature hybrid has to be equal to the IL. The same condition applies to the 2DSIMC, therefore the split of the quadrature hybrid was optimized to be 3.2 dB for ports 1 to 2 which slightly increased the overall IL, as shown in Figure 4.10b. This phenomenon was already studied in chapter 2.

4.3 Mathematical Modelling vs Simulated Results

The ability to create pinpoint nulls in the embedded element pattern was proven theoretically in the previous section. The closed-form expression describing the behaviour of the circuitry was derived and a random null was placed to prove the concept. The next step was to model the circuit in HFSS using Floquet ports to create a unit cell environment and validate it with simulations of the 2D nulling for three scan angles.

Components like the quadrature hybrid, described by (28), and the Wilkinson power divider, described by (29), are modelled using ideal S-parameters but do not reflect the behavior of real components. In order to get a more accurate prediction of the null placement in the mathematical model, simulated non-ideal components,

shown in Figure 4.10a and Figure 4.11a are imported directly from HFSS using S-parameters. Those S-parameters are then incorporated directly into the mathematical model. Since it was proven that a null can be steered using conventional phase shifters, varying lengths of line were used in the 2DSIMC to steer the null. This means that in order to demonstrate each null, an entire board containing the SIMC layer needs to be fabricated and tested. Therefore, three angles of null placements are selected strategically to prove the 2DSIMC concept and show the ability to steer the null in any direction. The first null is going to be placed directly at broadside $(\theta_1, \phi_1) = (0, 0)$. Another null is located at $(\theta_2, \phi_2) = (30, 0)$ to show that a 2D null can be steered in only one dimension. The third null is located away from broadside in both θ and ϕ angles for $(\theta_3, \phi_3) = (-45, 45)$. The spatial responses of the mathematical model for those angles are shown in Figure 4.12, where the antenna is substituted by a port to de-embed the 2DSIMC from the antenna and obtain isolated performance. The left column of Figure 4.12 represents the spatial response of the math model for previously mentioned null placements. The right column is the spatial response of the HFSS model of the same null placements as are shown in the left column. It can be observed that, in general, the IL is very similar in both columns, but the depth of the null is less in the HFSS simulated model.

Nulls of more than 25 dB are achieved when the S-parameters of the simulated passive components are fed into the mathematical model. The nulls are 5 dB deeper than the ones obtained with HFSS. The IL is 0.8 dB for the most optimal angle in HFSS and closely matches the mathematical model. A better comparison can be made when the mathematical and simulated results are plotted in the same figure. Cuts of the main angles of interest were extracted with the goal of showing the null for both dimensions. If the previous cuts do not show the minimum IL, another trace is added for it (Figure 4.13).

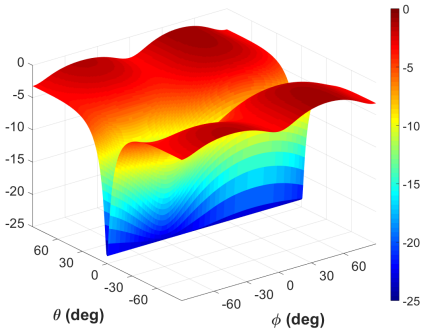

(a) MATH, null: $(\theta_1, \phi_1) = (0, 0)$

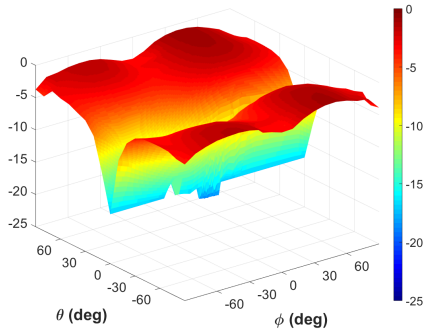

(b) HFSS, null: $(\theta_1, \phi_1) = (0, 0)$

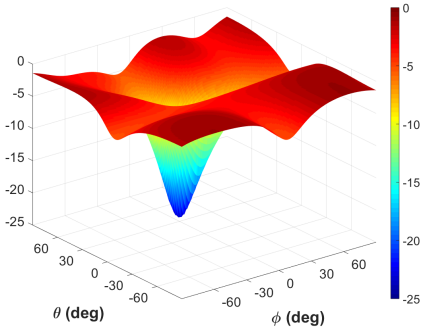

(c) MATH, null:$(\theta_2, \phi_2) = (30, 0)$

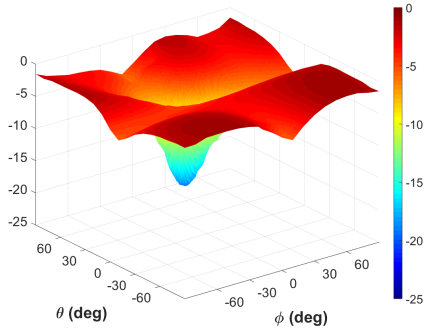

(d) HFSS, null:$(\theta_1, \phi_1) = (30, 0)$

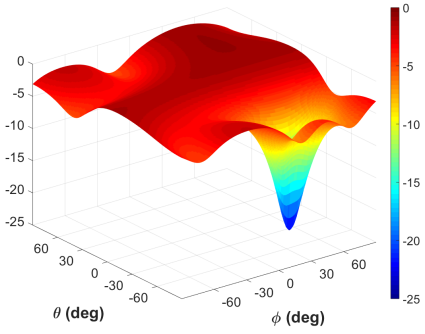

(e) MATH, null:$(\theta_3, \phi_3) = (-45, 45)$

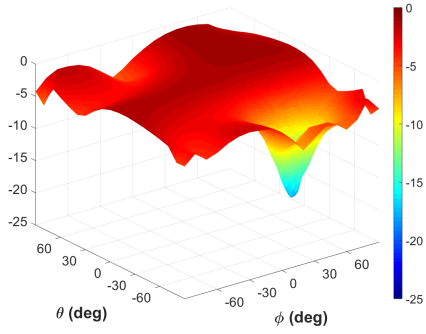

(f) HFSS, null:$(\theta_1, \phi_1) = (-45, 45)$

Figure 4.12: Results showing the spatial response of the signal going into the receiver (V_1^-) when using the 2DSIMC analytically (left column) and the simulated cases (right column).

It is important to note that the results plotted in Figure 4.12 show the performance of the 2DSIMC without the antenna. The IL for a certain angle varies depending on the null placement, and sometimes the angle of the least amount of IL

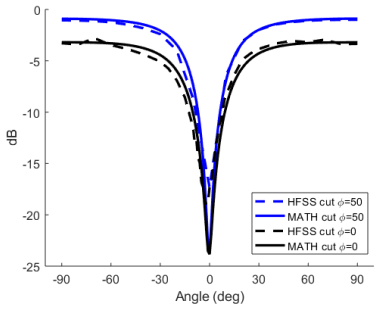

(a) Null at $(\theta_1, \phi_1) = (0, 0)$

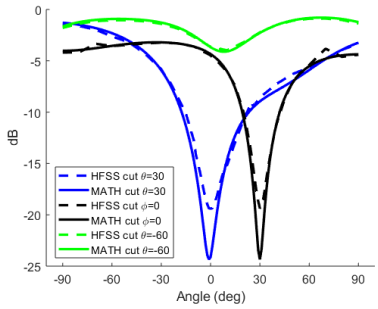

(b) Null at $(\theta_1, \phi_1) = (0, 0)$

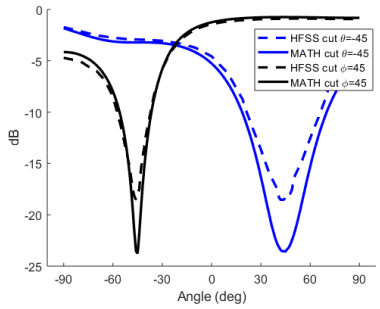

(c) Null at $(\theta_2, \phi_2) = (30, 0)$

Figure 4.13: Results showing the spatial response of the signal going into the receiver (V_1^-) when using the 2DSIMC when port 2 in (a) is excited. Three different null placements are shown, one for (b) the null at $(\theta_1, \phi_1) = (0, 0)$, (c) the null at $(\theta_2, \phi_2) = (30, 0)$, (d) and the null at $(\theta_3, \phi_3) = (-45, 45)$.

is "far" away from broadside. An example that illustrates this case is when the null is placed at $(\theta_2, \phi_2) = (30, 0)$ in Figure 4.13b, where the least amount of IL is at $60°$ away from broadside. That will not be the case when the 2DSIMC is connected to the antenna array because the gain of the antenna itself and the active reflection coefficient diminishes when scanning away from broadside. In the next section the overall performance of the 2DSIMC plus the antenna will be measured and compared to the simulated results of HFSS. The simulated results obtained with the 2DSIMC will be concatenated with the simulations of a naked patch antenna when placed in a unit cell.

4.4 7x7 Finite Array: Measured Results versus Simulated

An infinite array environment is convenient to calculate, simulate, and obtain close approximations of the antenna behavior when it is placed in a finite large array. In order to obtain measured results, a finite array needs to be fabricated. The constraints of the design were limited to allow for in-house fabrication that used standard sample board sizes of $12"x9"$ manufactured by Rogers. Simultaneously, the unit-cell needs to be big enough to hand-solder the components while still populated with enough elements so that the center one behaves similarly to an element placed in an infinite array. After combining previous constraints, it was determined that the array dimensions had to be 7x7 and operate at 5.5 GHz with a $\lambda/2$ element spacing ($\sim 27mm$). The center element of the array is located at (4,4) in Figure 4.2. That element is far away enough from the edges to avoid edge-effects of the array while at the same time being surrounded with the same amount of elements in all directions.

In the previous section it was shown that simulated results match closely with the analytical model. The unit cell was then duplicated 7 times in both dimensions in order to populate a full 7x7 array. The edge elements, the ones that do not adjacent elements, are terminated with 50 loads to absorb all the possible reflections from the signals that flow through the 2DSIMC circuitry.

In order to measure and compare the results with the those obtained in the previous section, 3 boards were fabricated, each containing one null. Those nulls are placed at $(\theta_1, \phi_1) = (0, 0)$, $(\theta_2, \phi_2) = (30, 0)$ and at $(\theta_3, \phi_3) = (-45, 45)$ degrees as shown in Figure 4.14, which contain the same null placements as the ones simulated in the previous section. The board that contains the null placed at $(0, 0)$ is fabricated in-house. A photolithography process was used to edge several redundant boards, but resulted in uneven edging for some elements. After measuring the

in-house board with the least fabrication errors for the null placed at $(0, 0)$, results were promising, so two additional boards designed for different null-placements were outsourced to improve fabrication consistency.

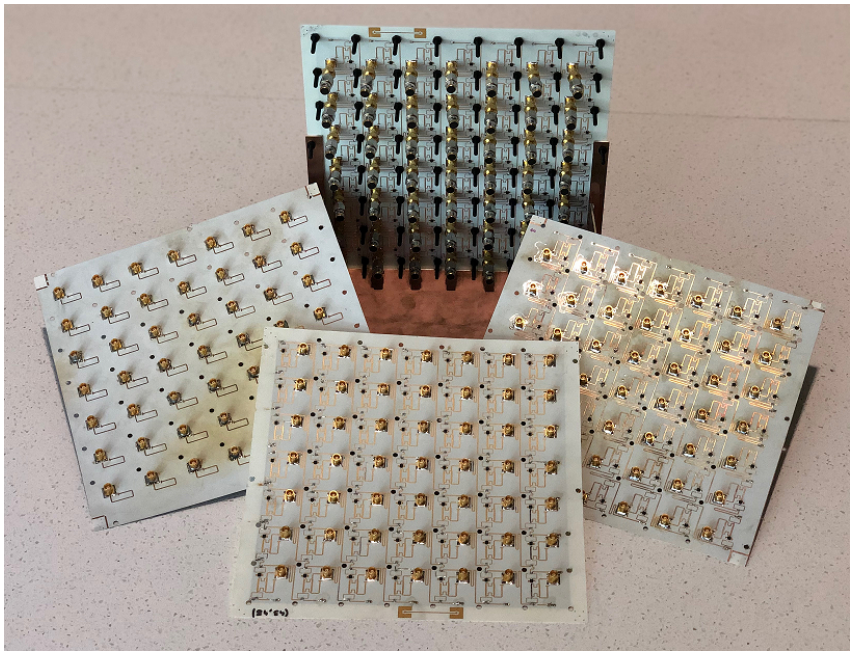

Figure 4.14: Depiction of three boards and how they are mounted on the antenna array.

A fourth board with only the feeding network and antenna was fabricated. This board acts as a reference to measure the IL of the 2DSIMC. The next figures will show the measured results of the system by displaying the critical embedded element patterns. All of the element patterns were measured in the anechoic chamber, as shown in Fig 4.15. The results show the embedded pattern of the center element of the array.

Both Figure 4.16a and Figure 4.16b show a very deep, sharp measured null with respect to the simulated one. In general, the board was slightly over-edged causing a reduction in the width of the lines. The slight reduction in width will not have much of an impact on the 50Ω transmission lines that interconnect components,

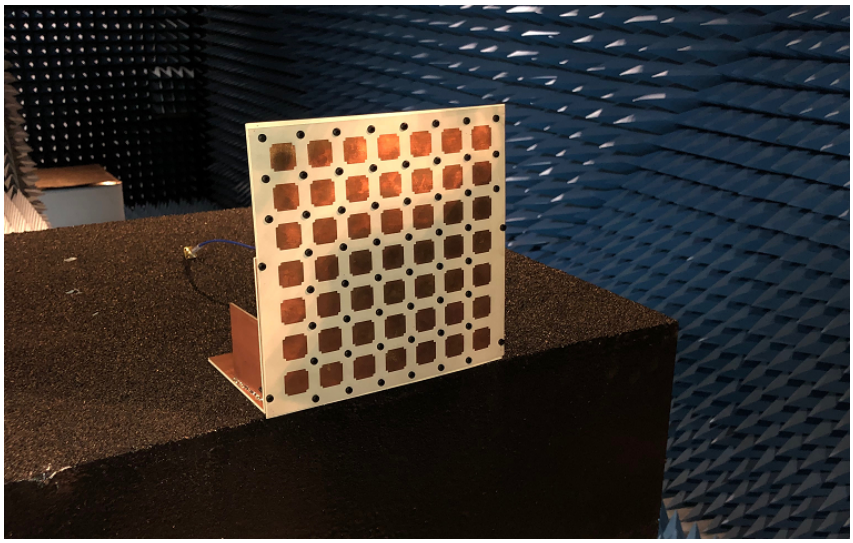

Figure 4.15: An illustration of the antenna array in the anechoic chamber.

but it will change the power splitting of the carefully fine-tuned unequal quadrature hybrid. For this board the line reduction worked to its advantage by creating finer and deeper nulls than were obtained using the other two boards.

When comparing the other HFSS results (right column) and measured results (left column) from the center element in Figure 4.16, it can be seen that the shape of the patterns do match in magnitude but the angles are off by $\pm 5^{\circ}$. In theory the center element is the one that most closely approximates the large array environment. However, the elements that provide the cancelling signal are not in the center element, and therefore provide this unit-cell versus finite array measurement miss-match. Thus, there is a chance that other array elements may perform more similarly to the infinite array environment when situated a little deeper into the array (positions > 4). There might also be a chance that fabrication imperfections can have an influence on the null placement. An example of this is that when there is a difference of 0.15 mm in transmission line length, the null will be off by 1°. Extra soldering, blind ground soldering, and hand-precision placements might all contribute to errors, especially when all elements are interconnected and there is no

easy way to see which one is failing.

It is observed from Figure 4.13 that the overall loss of the 2DSIMC is greater than that of the SIMC for linear arrays, making reduction of the IL of S_{12a} even more necessary. Figure 4.17 shows the great improvement of performance when the IL of the two-port network is reduced from 3 dB to 1 dB.

The next chapter will focus on a practical implementation of the SIMC that reduces the overall IL of the S_{12a} and improves the noise figure for the pass angles, as well as reducing the width of the nulls. The general two-port network is replaced by a tunable filter. When changing the center frequency of a filter, the phase changes for a particular frequency. This means that a tunable filter can act as a phase shifter. Filters can have low IL, especially when high Q resonators are used. The next chapter focuses on introducing a two-pole microstrip filter that is swapped for the phase shifter. The resulting improvement is shown in simulations.

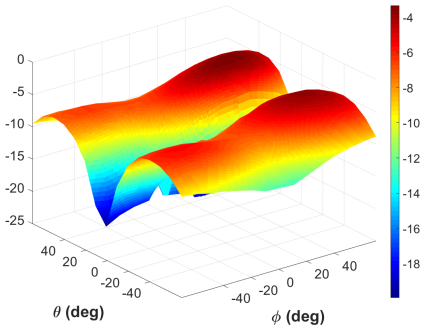

(a) HFSS, null: $(\theta_1, \phi_1) = (0, 0)$

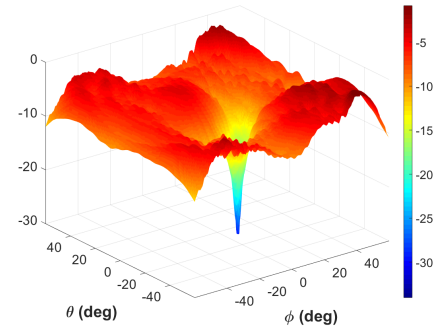

(b) measured, null: $(\theta_1, \phi_1) = (0, 0)$

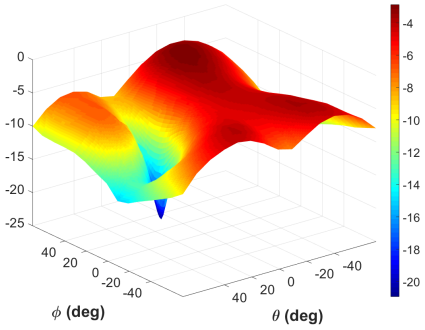

(c) HFSS, null:$(\theta_2, \phi_2) = (30, 0)$

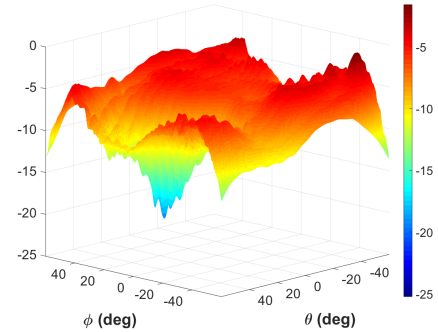

(d) measured, null:$(\theta_1, \phi_1) = (30, 0)$

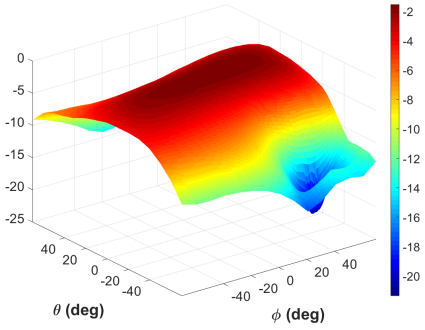

(e) HFSS, null:$(\theta_3, \phi_3) = (-45, 45)$

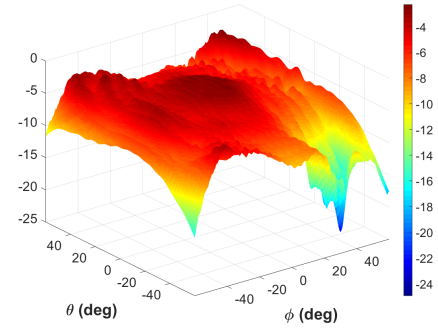

(f) measured, null:$(\theta_1, \phi_1) = (-45, 45)$

Figure 4.16: The spatial response of the 2DSIMC for the measured results (left column) and simulated results (right column).

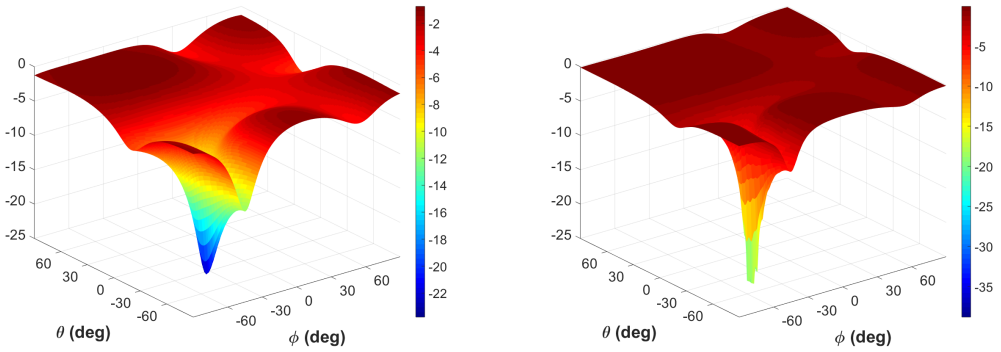

(a) Performance of 2DSIMC for $S_{12a} = 3$ dB

(b) Performance of 2DSIMC for $S_{12a} = 1$ dB

Figure 4.17: Illustration of the spatial response of the 2DSIMC for (a) $S_{12a} = 3$ dB and (b) $S_{12a} = 1$ dB. A clear improvement can be seen when using a lower IL two-port network.

5 SIMC with Tunable Filters

After successfully placing spatial nulls for linear arrays and planar arrays in order to mitigate spatial interferers, it was obvious that there was a need to increase the performance of the SIMC. This proved especially true for the 2DSIMC when an equal power split was used, as it produced multiple angles of (θ, ϕ) that were above 3 dB of IL (Figure 4.17). A negative impact on the receiver system occurs when many angles outside of the null have a high IL because they increase the overall noise figure and decrease the sensitivity. As mentioned in previous chapters, a decrease in the width of the null results in improved interferer-free scanning volume.

The closed-form expression derived for the SIMC and 2DSIMC states that the phase of the two-port network has to change in order to steer the null. In chapter 2 a phase shifter was used to change the phase and steer the null. The problem was that the phase shifter had more than 7 dB of IL and increased the overall noise figure. It proved to be very difficult to find a phase shifter with less than 3 dB of IL.

Chapter 1 mentioned that an advantage of fully digital arrays is that there is no need for costly phase shifters. Therefore, using phase shifters for null steering is generally in opposition to the trend of removing them from future digital arrays. Optional structures that could overcome the drawbacks of phase shifters are tunable filters. Tunable filters with a high Q provide a very low IL. When the center frequency of a tunable filter changes, the phase for a specific frequency at the pass band changes as well, therefore resulting in a phase shift.

5.1 The Analysis of Ideal Filters and Their Effects on the SIMC

Besides IL, another parameter that defines the tunable filter is the total range in terms of phase. Different ideal filter responses were analyzed. Microwave Office (AWR) was used to generate filter configurations and determine the phase differ-

ences for their tunable ranges. Each filter configuration was investigated by varying the BW, IL, order, and the type of response (Chebyshev or Butterworth). The only parameter that mattered for phase shifting purposes was the order of the filter. The higher the order of the filter, the higher the group delay (because each pole adds 90° of delay). Figure 5.1a and Figure 5.1b show the typical magnitude response of the filter for a 3rd and 5th order filter. A higher group delay translated into an increased phase slope in the frequency response, as shown in Figure 5.1c and Figure 5.1d. That delay is directly related to a phase shift. Therefore, for an equal tuning range in frequency, a higher order filter equates to a higher phase shifting range. For example, if the system operates at 2.75 GHz, from Figure 5.1c and 5.1d it can be seen that at 2.75 GHz, a higher variation in phase shift was achieved for the 5th order filter. For a $\lambda/2$ element spacing the $\Delta phase$ only needs to range between $[0, 2\pi]$ to allow a full 180° null steering.

Figure 5.1e and Figure 5.1f illustrate the spatial response of the voltage going into the receiver when the two-port network is a 3rd or 5th order filter. Since the schematic is the same as the one in chapter 2, the same closed-form expression derived in (15) is used to plot the spatial response of the different filter configurations. As expected, the 5th order filter offers 180° null placement which is higher than the 60° range offered by the 3rd order. The spatial response is obtained after adding a 3 dB attenuator to the ideal filter and preserving the equal split quadrature hybrid. This procedure was done because it was of interest only to observe the angular range of the null placement and the frequency response for the ideal case. A higher slope of the phase versus frequency implies that the change of phase shift of the filter is more sensitive to frequency. Since there is an exact value needed for locating a null in a certain angle, any change in phase will change the null placement. This directly impacts the bandwidth of the null as shown in Figure 5.2 where

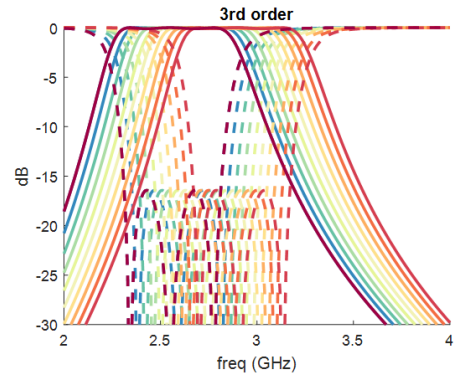

(a) magnitude response 3rd order

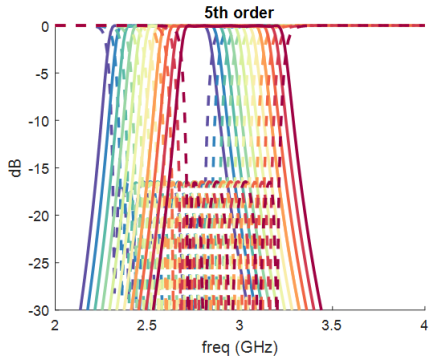

(b) magnitude response 5rd order

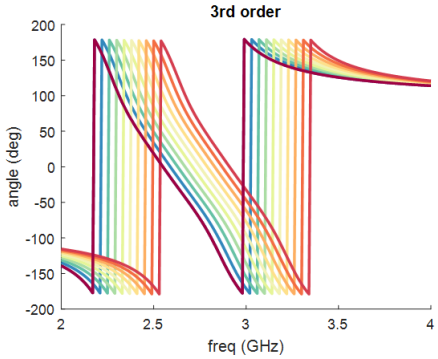

(c) phase response 3rd order

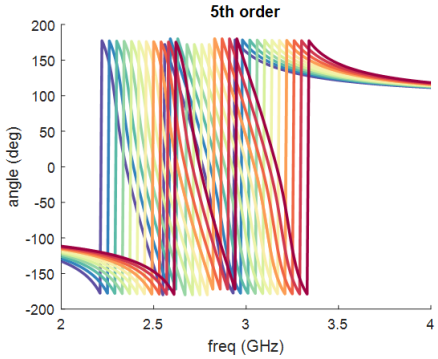

(d) phase response 5th order

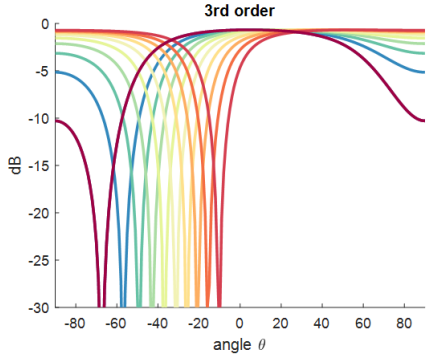

(e) SIMC spatial response 3rd order

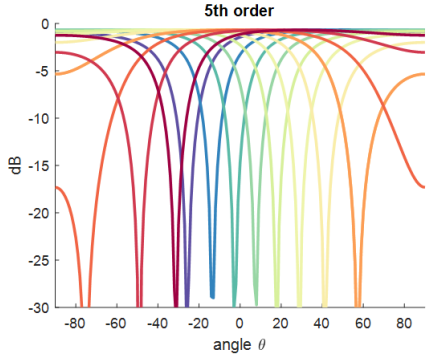

(f) SIMC spatial response 5th order

Figure 5.1: Results showing the magnitude, phase, and the SIMC response for the 3rd order filter (right column) and 5th order filter (left column).

the 5th order has a narrower null in the frequency domain than the 3rd order filter. This means that there is a compromise between the range of the null placement and the bandwidth of the filter. Another aspect that needs to be taken into account is

that in a real situation, a 5th order filter will have a higher IL than a 3rd order filter. Therefore, the order of the filter needs to be carefully selected when designing the SIMC for a real system. The IL analysis is discussed in the next subsections.

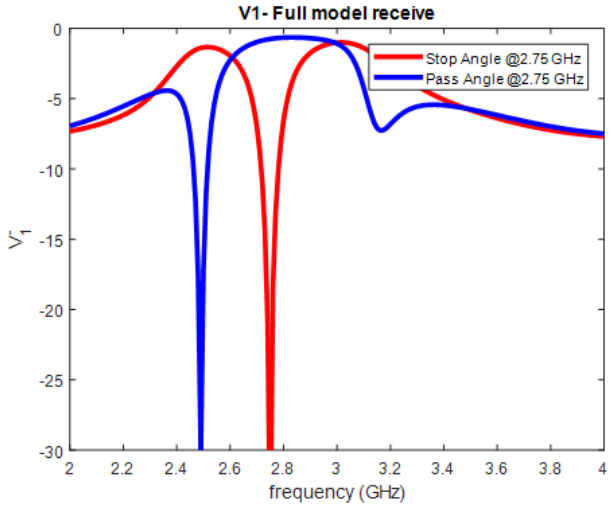

(a) frequency response 3rd order

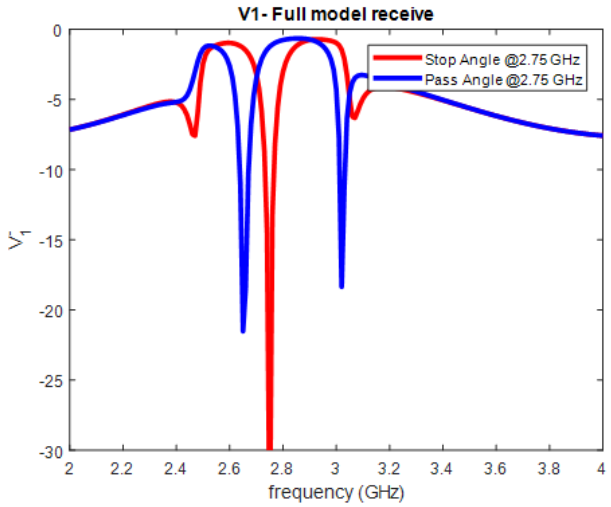

(b) frequency response 5rd order

Figure 5.2: The frequency response of the SIMC for the pass angle and stop angle of (a) a 3rd order filter and (b) a 5th order filter.

The effective tuning range that can be used in the SIMC is limited by the bandwidth of the passband of the filter. The cancelling signal needs to flow through

the passband of the filter, otherwise all the power will be reflected back into the receiver.

Thus far, this subsection has proven that an ideal filter can change the null placement. The phase-slope determines the angular null placement range and the bandwidth of the null. In order to prove the concept of using a tunable filter as a phase shifter, the next subsection will discuss using a two-pole microstrip filter that was designed and simulated in HFSS. Successful results in terms of IL and of null steering are shown when the filter is integrated in the SIMC.

5.2 Null Steering with Tunable Microstrip Filter

In the previous section it has been proven that a filter can theoretically replace the phase shifter and change the null placement of the SIMC. A two-pole tunable filter implementation would be enough to prove the concept of null steering while simultaneously reducing the overall IL. The 3D model of the two-pole varactor diode filter is shown below in Figure 5.3a. The filter is designed on a 30 mil Rogers 4350B substrate. A varactor diode is a component that changes its capacitance when biased with different DC voltages. From transmission line theory, a change of capacitance before a short circuit may be used to change the equivalent electric length. By manipulating the electric length of a resonator, the resonant frequency varies and so does the center frequency of the filter, resulting in a phase shift.

Figure 5.3b shows the resulting frequency response of the filter using three different varactor capacitance configurations (C). The filter response for a $C = 0.975$ pF (blue line) shows how the lower end of the pass band is at the operating frequency of the SIMC, 2.75 GHz. The red line ($C = 0.825$ pF) shows how the higher end of the pass band is at the SIMC's operating frequency. These two responses represent the tunable range of this particular filter when integrated into the SIMC.

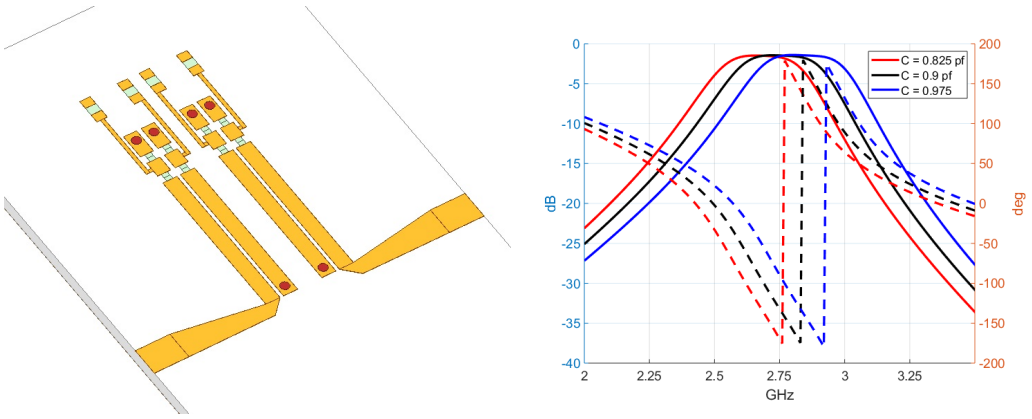

(a) 3D model

(b) frequency response

Figure 5.3: A depiction of (a) the 3D model of the two-pole varactor tuned microstrip filter and (b) the frequency response of the filter from port 1 to 2. Solid lines represent the magnitude and dashed lines represent the phase delay.

The black line is the filter's frequency response when the varactor is tuned at 0.9 pF. At that configuration, the center of the pass band of the filter is at the center of the SIMC's operating frequency. The simulated IL of the pass band is 1.5 dB. As derived from (25) in chapter 2), S_{12}, the quadrature hybrid power split can be increased from 3 dB to 1.5 dB and the overall IL can be dramatically improved. The total range in phase of the 2nd order filter is $60°$ at 2.75 GHz and is illustrated in Figure 5.3b with dashed lines. The analytical model predicts a null placement range from $\pm 13°$. This nulling range might not be enough for a general practical application; however, it does show that null steering can be accomplished. In practical real-world applications, a more complex filter design that provides a wider range in phase shifting should be implemented.

5.3 Unit Cell of the SIMC Using a Tunable Microstrip Filter

It was demonstrated in the previous section that by using analytical models, a 2nd order tunable filter can steer the null. In order to validate those results, a unit cell will be designed in which the filter replaces the general two-port network (Figure

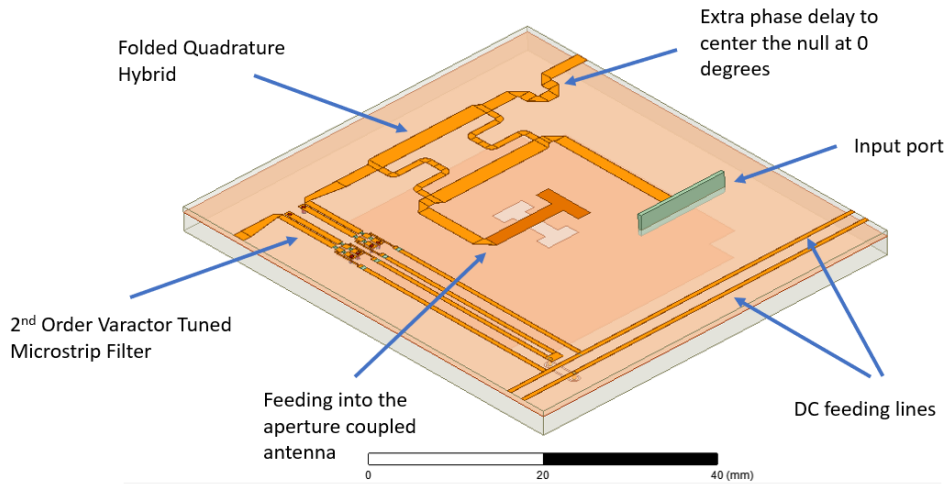

Figure 5.4: Illustration of the 3D model of the SIMC with a tunable filter placed in a unit cell.

5.4). The SIMC layer is designed for a 30 mil Rogers 4350B, the quadrature hybrid is folded to optimize the layout, and the operating frequency is set at 2.75 GHz with the spacing between elements at $\lambda/2$.

To match the IL of the filter with the losses produced by the transmission lines and soldering, the quadrature hybrid is redesigned such that $S_{12} = -1.8$ dB. In order to center the null at $\theta = 0$ for the spatial response at $C = 0.9$ pF, extra transmission line length is added as shown in Figure 5.4. This allows for the SIMC to place a null symmetrically in θ. To evaluate the performance of the SIMC, it is best to de-embed the antenna. The antenna and its aperture coupled feeding structure is replaced by a port. The simulated results of the spatial response of the SIMC with the filter are shown in Figure 5.5a and are compared to the spatial response provided by the mathematical model for a two-port network.

The difference in IL is only 0.15 dB between the mathematical model and simulated results, a close match. As predicted in chapter 2, the IL is reduced from 0.8 dB for an equal split to 0.4 dB, and a significantly narrower null is observed. Figure

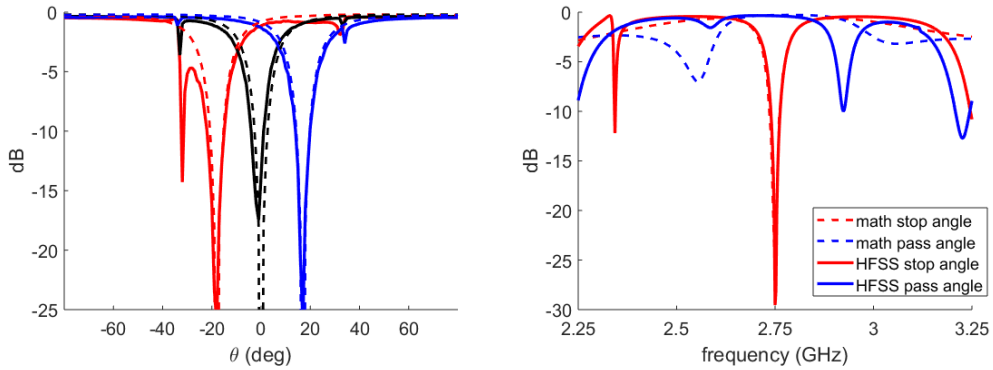

(a) Spatial response

(b) frequency response for C = 0.9 pF

Figure 5.5: An illustration of the SIMC with the filter where (a) the spatial response is shown and (b) the frequency response for $C = 0.9$ pF.

5.5b shows the frequency response of the SIMC with the filter for the pass angle and stop angle. The measured result and mathematical model seem to mirror each other. Future work will try to solve this divergence. The null has a 3 dB fractional bandwidth of 1.6%, currently making the SIMC suitable for narrowband interference. Simulated results confirm that the tunable filter can steer the null and the spatial response can be accurately predicted with the analytical model. The next step will be to fabricate a linear 10 element array and measure the embedded element patterns.

6 Conclusions and Future Work

6.1 Conclusions

This work presents an antenna agnostic spatial interference mitigation circuit (SIMC). This circuit interconnects antenna elements and creates an artificial steerable null in the embedded element pattern, significantly mitigating the interference at the RF front-end before it enters the receiver. This technique prevents jammers or other strong interferers from corrupting the sensitive components in the receiver chain. A complete mathematical model of this circuitry is presented and is proven to accurately predict the behavior of the SIMC in a large array environment. A closed-form expression to steer the null at a specified incoming angle is derived. In order to validate the mathematical model, simulated and experimental results are obtained for a 1x8 array. As a proof of concept, measurements were taken in an anechoic chamber and embedded element patterns with nulls of more than 20 dB were measured. When the array pattern is measured and calculated for a 1x8 array, the performance is decreased because the first element, the one that has no cancellation signal, does not have any spatial mitigation and decreases the performance of the small array. Large arrays, especially the ones that are populated with dummy elements, should not be affected by the performance of the first element. Finally, a discussion of a system-level demonstration with fully tunable nulling circuitry is provided. The procedure included an interferer that initially prevented the demodulation of the SoI. The interferer was successfully mitigated allowing the receiver to demodulate the SoI.

The linear array was able to place a null, but only in one dimension. The null cuts a whole angular plane that mitigates the interferer, but also other possible important information that is contained within the plane. In order to address this

possible loss of information, the circuitry is expanded and adapted to a planar array 2DSIMC which allows for providing a 2D null. 2D nulling allows maximizing the interferer-free scanning volume. The spatial response of the 2D nulling accentuated the need to optimize the overall IL over the pass angle.

This work shows how the overall IL of the SIMC can be decreased substantially by using a low-loss tunable two-port network. The traditional phase shifter was substituted with a tunable microstrip filter. It was shown that in addition to improving the overall IL of the SIMC, the spatial null gets narrower, resulting in improvement of the spatial selectivity and increasing the interferer-free scanning volume.

6.2 Future Work

Future research should include the fabrication and measurements of a linear SIMC filter array. Another relevant problem to solve is determining a method to place a null in the embedded pattern of the first element, the one that does not have a cancelling signal because there is no adjacent element. The solution could be as simple as feeding the cancelling signal of the last element into the first one instead of terminating them. This would mean that all elements should perform exactly the same and approximate the unit-cell response. Interconnection of just two elements could achieve an infinite array response. Having just two elements that provide an infinite array response would make modular design easier and provide better results. This structure needs to be carefully analyzed for grating lobes, because with the proposed changes, the unit cell dimension increases to λ.

A more difficult challenge to solve is how to mitigate multiple interferers. The author of this work believes there will be an amplification stage needed in the SIMC in order to provide the cancelling signal for multiple interferers. The advantages of amplification could include a reduction in overall IL. At the same time, adding amplifiers introduces complexity and a possibility that they will operate into the non-linear region and decrease the overall dynamic range. This trade-off needs to be carefully analyzed.

Also of value for future investigation would be increasing the bandwidth of the null so that the circuitry functions for wide-band interferers. A different two-port network/coupling structure might prove of value for the purpose of solving the bandwidth limitations.

References

[1] C. Fulton, "Digital array radar calibration and performance monitoring techniques for direct conversion and dual polarization", PhD thesis, Purdue University, 2011.

[2] C. Fulton, M. Yeary, D. Thompson, J. Lake, and A. Mitchell, "Digital Phased Arrays: Challenges and Opportunities", *Proceedings of the IEEE*, vol. 104, no. 3, pp. 487–503, 2016, ISSN: 00189219. DOI: 10.1109/JPROC.2015.2501804.

[3] W. Chappell and C. Fulton, "Digital Array Radar panel development", *IEEE International Symposium on Phased Array Systems and Technology*, pp. 50–60, 2010. DOI: 10.1109/ARRAY.2010.5613391.

[4] J. M. Loomis, "Army radar requirements for the 21st century", *IEEE National Radar Conference - Proceedings*, pp. 1–6, 2007, ISSN: 1097-5659. DOI: 10.1109/RADAR.2007.374182.

[5] C. Fulton, P. Clough, V. Pai, and W. Chappell, "A digital array radar with a hierarchical system architecture", *IEEE MTT-S International Microwave Symposium Digest*, pp. 89–92, 2009, ISSN: 0149645X. DOI: 10.1109/MWSYM.2009.5165639.

[6] D. C. D. Chang, W. N. Klimczak, and G. C. Busche, "An experimental digital beamforming array", 1300–1303 vol.3, Jun. 1988.

[7] A. Garrod, "Digital modules for phased array radar", pp. 81–86, Oct. 1996. DOI: 10.1109/PAST.1996.565940.

[8] J. F. Rose, B. A. Worley, and M. M. Lee, "Antenna patterns for prototype two-dimensional digital beamforming array", 1544–1547 vol.3, Jun. 1993. DOI: 10.1109/APS.1993.385490.

[9] F. Catta-Preta, *Northrop Grumman and CEA Demonstrate Scalable CEAFAR Next-Generation Phased Array Sensor System*, 2011.

[10] I. A. Industries, *1st Deliveries of IAI Multi Function Surveillance Threat Alert Radar*, 2010.

[11] J. E. Stailey and K. D. Hondl, "Multifunction Phased Array Radar for Aircraft and Weather Surveillance", *Proceedings of the IEEE*, vol. 104, no. 3, pp. 649–659, 2016. DOI: 10.1109/JPROC.2015.2491179.

[12] T. Hoffmann, C. Fulton, M. Yeary, A. Saunders, D. Thompson, B. Murmann, B. Chen, and A. Guo, "Measured performance of the impact common module — a building block for next generation phase arrays", pp. 1–7, Oct. 2016. DOI: 10.1109/ARRAY.2016.7832593.

[13] C.J Fulton, J.Salazar, H. Sigmarsson, M. Yeary, R.D Palmer, "The 'Horus' Radar—An All-Digital Polarimetric Phased Array Radar for Multi-Mission Surveillance, 99 th", *American Meteorological Society, Phoenix, January*, no. January 2019,

[14] H. Saeidi-Manesh and G. Zhang, "High-isolation, low cross-polarization, dual- polarization, hybrid feed microstrip patch array antenna for mpar application", *IEEE Transactions on Antennas and Propagation*, vol. 66, no. 5, pp. 2326–2332, May 2018, ISSN: 0018-926X.

[15] A. Mancini, R. M. Lebrón, and J. L. Salazar, "The impact of a wet s -band radome on dual-polarized phased-array radar system performance", *IEEE Transactions on Antennas and Propagation*, vol. 67, no. 1, pp. 207–220, Jan. 2019, ISSN: 0018-926X. DOI: 10.1109/TAP.2018.2876733.

[16] J. G. Andrews, S. Buzzi, W. Choi, S. V. Hanly, A. Lozano, A. C. K. Soong, and J. C. Zhang, "What will 5g be?", *IEEE Journal on Selected Areas in Communications*, vol. 32, no. 6, pp. 1065–1082, Jun. 2014, ISSN: 0733-8716. DOI: 10.1109/JSAC.2014.2328098.

[17] L. Zhang, A. Natarajan, and H. Krishnaswamy, "Scalable Spatial Notch Suppression in Spatio-Spectral-Filtering MIMO Receiver Arrays for Digital Beamforming", *IEEE Journal of Solid-State Circuits*, vol. 51, no. 12, pp. 3152–3166, 2016, ISSN: 00189200. DOI: 10.1109/JSSC.2016.2600579.

[18] S. H. Talisa, K. W. O'Haver, T. M. Comberiate, M. D. Sharp, and O. F. Somerlock, "Benefits of Digital Phased Array Radars", *Proceedings of the IEEE*, vol. 104, no. 3, pp. 530–543, 2016, ISSN: 00189219. DOI: 10.1109/JPROC.2016.2515842.

[19] J. H. C. van den Heuvel, J. M. G. Linnartz, P. G. M. Baltus, and D. Cabric, "Full mimo spatial filtering approach for dynamic range reduction in wideband cognitive radios", *IEEE Transactions on Circuits and Systems I: Regular Papers*, vol. 59, no. 11, pp. 2761–2773, Nov. 2012, ISSN: 1549-8328. DOI: 10.1109/TCSI.2012.2189056.

[20] C. Kim, S. Joshi, C. M. Thomas, S. Ha, L. E. Larson, and G. Cauwenberghs, "A 1.3 mW 48 MHz 4 Channel MIMO Baseband Receiver With 65 dB Har-

monic Rejection and 48.5 dB Spatial Signal Separation", *IEEE Journal of Solid-State Circuits*, vol. 51, no. 4, pp. 832–844, 2016, ISSN: 00189200. DOI: 10.1109/JSSC.2016.2519398.

[21] N. Peccarelli, S. Member, B. James, S. Member, R. Irazoqui, S. Member, J. Metcalf, C. Fulton, and S. Member, "Survey : Characterization and Mitigation of Spatial / Spectral Interferers and Transceiver Nonlinearities for 5G MIMO Systems", *IEEE Transactions on Microwave Theory and Techniques*, pp. 1–18, 2019.

[22] B. James and C. Fulton, "Decorrelation and mitigation of spurious products in phased arrays with direct conversion transceivers", *2015 IEEE MTT-S International Microwave Symposium, IMS 2015*, pp. 1–3, 2015. DOI: 10.1109/MWSYM.2015.7166990.

[23] N. Peccarelli and C. Fulton, "Adaptive Nonlinear Equalization of a Tunable Bandpass Filter", *IEEE Microwave and Wireless Components Letters*, vol. 29, no. 2, pp. 149–151, 2019, ISSN: 15311309. DOI: 10.1109/LMWC.2018.2887387.

[24] D. M. Pozar, *Microwave engineering; 3rd ed.* Hoboken, NJ: Wiley, 2005.

[25] S. Zhang, G. H. Huff, J. Feng, and J. T. Bernhard, "A pattern reconfigurable microstrip parasitic array", *IEEE Transactions on Antennas and Propagation*, vol. 52, no. 10, pp. 2773–2776, Oct. 2004, ISSN: 0018-926X. DOI: 10.1109/TAP.2004.834372.

[26] Run-Liang Xia, Shi-Wei Qu, Ming-Yao Xia, and Zai-Ping Nie, "Wide-angle impedance matching of phased-array antenna using overlapped subarrays",

Proceedings of the International Symposium on Antennas & Propagation, vol. 01, no. c, pp. 508–511, 2013.

[27] Z. Li, E. Ahmed, A. M. Eltawil, and B. A. Cetiner, "A beam-steering reconfigurable antenna for WLAN applications", *IEEE Transactions on Antennas and Propagation*, vol. 63, no. 1, pp. 24–32, 2015, ISSN: 0018926X. DOI: 10.1109/TAP.2014.2367500.

[28] M. A. Towfiq, I. Bahceci, S. Blanch, J. Romeu, L. Jofre, and B. A. Cetiner, "A reconfigurable antenna with beam steering and beamwidth variability for wireless communications", *IEEE Transactions on Antennas and Propagation*, vol. 66, no. 10, pp. 5052–5063, Oct. 2018, ISSN: 0018-926X. DOI: 10.1109/TAP.2018.2855668.

[29] Y. F. Cheng, X. Ding, W. Shao, M. X. Yu, and B. Z. Wang, "A Novel Wide-Angle Scanning Phased Array Based on Dual-Mode Pattern-Reconfigurable Elements", *IEEE Antennas and Wireless Propagation Letters*, vol. 16, pp. 396–399, 2017, ISSN: 15361225. DOI: 10.1109/LAWP.2016.2580624.

[30] N. H. Chamok, M. H. Yilmaz, H. Arslan, and M. Ali, "High-Gain Pattern Reconfigurable MIMO Antenna Array for Wireless Handheld Terminals", *IEEE Transactions on Antennas and Propagation*, vol. 64, no. 10, pp. 4306–4315, 2016, ISSN: 0018926X. DOI: 10.1109/TAP.2016.2598201.

[31] M. A. Hossain, I. Bahceci, and B. A. Cetiner, "Parasitic layer-based radiation pattern reconfigurable antenna for 5g communications", *IEEE Transactions on Antennas and Propagation*, vol. 65, no. 12, pp. 6444–6452, Dec. 2017, ISSN: 0018-926X. DOI: 10.1109/TAP.2017.2757962.

[32] J. Butler and R. Rowe, "Beamforming matrix simplifies design of electronically scanned antennas", *Electron*, vol. 9, pp. 170–173, 1961.

[33] W. Li, C. Chu, K. Lin, and S. Chang, "Switched-beam antenna based on modified butler matrix with low sidelobe level", *Electronics Letters*, vol. 40, no. 5, pp. 290–292, Mar. 2004, ISSN: 0013-5194. DOI: 10.1049/el:20040198.

[34] J. Remez and R. Carmon, "Compact designs of waveguide Butler matrices", *IEEE Antennas and Wireless Propagation Letters*, vol. 5, no. 1, pp. 27–31, 2006, ISSN: 15361225. DOI: 10.1109/LAWP.2005.863615.

[35] K. Wincza and S. Gruszczynski, "Miniaturized broadband 4×4 Butler matrix designed with the use of quasi-lumped coupled-line couplers", *2012 8th International Caribbean Conference on Devices, Circuits and Systems, ICCDCS 2012*, pp. 1–4, 2012. DOI: 10.1109/ICCDCS.2012.6188906.

[36] L. Zhang and H. Krishnaswamy, "Supporting Analog / RF Arbitrary Spatial Filtering", *IEEE International Solid-state Circuits Conference*, no. i, pp. 410–412, 2017. DOI: 10.1109/ISSCC.2017.7870435.

[37] S. Jain, Y. Wang, and A. Natarajan, "A 10GHz CMOS RX frontend with spatial cancellation of co-channel interferers for MIMO/digital beamforming arrays", *Digest of Papers - IEEE Radio Frequency Integrated Circuits Symposium*, vol. 2016-July, pp. 99–102, 2016, ISSN: 15292517. DOI: 10.1109/RFIC.2016.7508260.

[38] D. Murphy, H. Darabi, A. Abidi, A. A. Hafez, A. Mirzaei, M. Mikhemar, and M. C. F. Chang, "A blocker-tolerant, noise-cancelling receiver suitable

for wideband wireless applications", *IEEE Journal of Solid-State Circuits*, vol. 47, no. 12, pp. 2943–2963, 2012, ISSN: 00189200. DOI: 10.1109/JSSC.2012.2217832.

[39] S. M. Duffy, G. A. Brigham, and J. S. Herd, "Integrated compensation network for low mutual coupling of planar microstrip antenna arrays", *IEEE Antennas and Propagation Society, AP-S International Symposium (Digest)*, no. 1, pp. 1389–1392, 2007, ISSN: 15223965. DOI: 10.1109/APS.2007.4395763.

[40] P. Hannan, D. Lerner, and G. Knittel, "Impedance matching a phased-array antenna over wide scan angles by connecting circuits", *IEEE Transactions on Antennas and Propagation*, vol. 13, no. 1, pp. 28–34, 1965, ISSN: 0096-1973. DOI: 10.1109/TAP.1965.1138365.

[41] R. L. Xia, S. W. Qu, P. F. Li, D. Q. Yang, S. Yang, and Z. P. Nie, "Wide-Angle Scanning Phased Array Using an Efficient Decoupling Network", *IEEE Transactions on Antennas and Propagation*, vol. 63, no. 11, pp. 5161–5165, 2015, ISSN: 0018926X. DOI: 10.1109/TAP.2015.2476342.

[42] Oliner and G.H. Knittel, *Phased Array Antennas*. 1972, ISBN: 9780471727576.